Dynamic simulation of structural phase transitions in magnetic iron

Pui-Wai Ma* and S. L. Dudarev
Culham Centre for Fusion Energy, Abingdon, Oxfordshire OX14 3DB, United Kingdom

Jan S. Wróbel
Division of Materials Design, Faculty of Materials Science and Engineering, Warsaw University of Technology, Wołoska 141, 02-507 Warsaw, Poland

(Received 13 June 2017; revised manuscript received 7 August 2017; published 18 September 2017)

The occurrence of bcc-fcc (α-γ) and fcc-bcc (γ-δ) phase transitions in magnetic iron stems from the interplay between magnetic excitations and lattice vibrations. However, this fact has never been confirmed by a direct dynamic simulation, treating noncollinear magnetic fluctuations and dynamics of atoms, and their coupling at a finite temperature. Starting from a large set of data generated by *ab initio* simulations, we derive noncollinear magnetic many-body potentials for bcc and fcc iron, describing fluctuations of atomic coordinates in the vicinity of near perfect lattice positions. We then use spin-lattice dynamic simulations to evaluate the difference between the free energies of bcc and fcc phases, assessing their relative stability within a unified dynamic picture. We find two intersections between the bcc and fcc free energy curves, which correspond to the α-γ bcc-fcc and γ-δ fcc-bcc phase transitions. The maximum bcc-fcc free energy difference over the temperature interval between the two phase transitions is 2 meV per atom, in agreement with other experimental and theoretical estimates.

DOI: 10.1103/PhysRevB.96.094418

I. INTRODUCTION

Pure iron undergoes bcc-fcc (α-γ) and fcc-bcc (γ-δ) phase transitions at temperatures $T_{\alpha\text{-}\gamma} = 1185$ K and $T_{\gamma\text{-}\delta} = 1667$ K, respectively. They occur in the interval between the Curie temperature $T_C = 1043$ K and the melting temperature $T_M = 1811$ K. These transitions have exceptionally significant practical implications as they are responsible for the formation of martensite in steels, and hence represent the most fundamental phenomena underpinning steel manufacturing and modern metallurgy. It has long been speculated that α-γ-δ phase transitions in iron stem from the interplay between magnetic excitations and lattice vibrations. Still, there is no evidence, derived from a direct simulation, confirming this assertion. The position is somewhat unsatisfactory as it leaves open the question of whether, using the available modern materials modeling concepts and algorithms, it is actually possible to discover a magnetism-driven structural phase transition by exploring the dynamics of a discrete atomistic model.

Hasegawa and Pettifor [1] investigated the relative stability of bcc, fcc, and hcp phases of iron as a function of temperature and pressure. They concluded that the relative stability of phases was primarily determined by the magnetic free energy contribution. Since they used a single-site spin-fluctuation approximation, which is a mean-field approach where the short-range magnetic order (SRMO) is neglected, the predicted phase diagram was rather qualitative than quantitative.

Recent experiments [2], which explored phonon dispersion in iron at high temperatures, showed that the stabilization of the high-temperature bcc δ phase is due primarily to vibrational entropy, whereas the fcc γ phase is stabilized by the fine balance between electronic and vibrational entropy contributions. This agrees with calculations performed using Monte Carlo magnetic cluster expansion (MCE) [3,4]. Although in the MCE the phonon contribution to the free energy is derived from experimental data, the MCE analysis shows that magnetic excitations change the sign of the free energy difference between the bcc and fcc phases $\Delta F^{\text{fcc-bcc}}$, and stabilize the γ phase. The bcc δ phase becomes more stable again at higher temperatures, because the lattice vibrational part of the free energy at high temperatures is greater than the part associated with magnetic excitations.

Several recent studies of the phase stability of iron are based on *ab initio* calculations [5–8] or the tight-binding Stoner model [6,7,9]. Most of them explore the stability of phases at 0 K, since this is a limitation associated with conventional applications of density functional theory (DFT). Treating magnetism in the framework of a tight-binding model is also not trivial since the fully noncollinear version of the tight-binding model Hamiltonian, including on-site interactions between electrons that gives rise to spin and orbital magnetism, has been derived only recently [10]. In principle, the Coury Hamiltonian [10] should enable fully self-consistent noncollinear magnetic dynamic simulations of atoms and magnetic moments, treated at the electronic scale.

Several approaches have been developed to describe finite-temperature magnetic excitations using *ab initio* techniques, see Ref. [11] for a review. The disordered local moments (DLM) [12–15] approximation assumes randomly distributed collinear up and down oriented magnetic moments, to imitate a fully magnetically disordered paramagnetic (PM) state of a material. It has been applied to modeling bcc-fcc [12] and bcc-hcp [15] transitions. To treat temperatures lower than T_C, where iron is in a partially ordered ferromagnetic (FM) state, partial or uncompensated DLM appromations [13–15] were proposed, where the net magnetization is constrained to a fixed value, matching experimental observations. This approach reproduces the elastic anisotropy of iron and Fe-Cr alloys [13]. However, the notion of SRMO remains undefined as the DLM approximation neglects magnetic noncollinearity.

*leo.ma@ukaea.uk

 ©2017 American Physical Society

Recently, Leonov *et al.* [16–18] investigated the stability of phases in iron using a combination of DFT and dynamic mean field theory (DMFT). The treatment involved an explicit consideration of temperature-dependent electron correlations. In the DMFT formalism, excitations associated with electron-electron interactions were treated using a single-site mean-field approximation, and neither collective magnetic excitations nor the SRMO were taken into account.

SRMO can be treated in the random phase approximation (RPA) combined with rescaling [19]. This approach was applied to evaluate magnetic, electronic and phonon contributions to the free energy, and also to assess the pressure dependence of T_C [20] in iron. The treatment has also been extended to quantum effects by rescaling the available classical solutions [21]. However, the mean-field nature of the approach gives rise to the predicted value of T_C that is higher than the observed value. An alternative approach to modeling SRMO is the spin-wave method [22].

SRMO can be simulated using *ab initio* spin dynamics (SD) [23–26] combined with constrained noncollinear calculations [27–32]. However, this is a computationally highly demanding approach, applicable only to relatively small systems. A more practical way of treating SRMO is to derive parameters from *ab intio* data and perform atomic scale SD [33,34] or Monte Carlo [3,4,35,36] simulations.

In the treatment of structural phase transitions, magnetic and phonon excitations, as well as coupling between them, appear significant. Körmann *et al.* proposed a spin space averaging procedure [37,38] to evaluate effective interatomic forces at a finite temperature by interpolating wave functions between the FM and PM states and performing statistical averaging over many magnetic microstates. The procedure was applied to modeling phonon spectra and changes in those spectra due to magnon-phonon interactions.

Conventional many-body interatomic potentials for molecular dynamics (MD) treat only the atomic degrees of freedom. Most of the potentials [39–43] are fitted to *ab initio* data at 0 K. Although some were successful [39] in reproducing bcc, fcc, and hcp phases at various temperatures and pressures, they required adjusting the energies of fcc and hcp structures to compensate for the absence of an explicit treatment of magnetic effects. Improvements in the functional forms of interatomic potentials were proposed [44–46], but they still did not include magnetic degrees of freedom explicitly, and did not treat thermal magnetic fluctuations.

There were partially successful attempts to incorporate magnetic states explicitly in MD. For example, Lian *et al.* [47] performed *ab initio* MD simulations to obtain phonon dispersion curves of γ and δ phases of iron over a range of temperatures. However, only the antiferromagnetic state (AFM) was used to represent the PM configuration. Alling *et al.* [48] performed DLM+MD to study the effect of atomic vibrations on magnetic properties. No equations of motion for magnetic moments were considered, and the dynamics of magnetic excitations was modeled as stochastic spin flips. This leads to conceptual difficulties in the treatment of thermalization of atoms and spins.

In this study, we use spin-lattice dynamics (SLD) [49,50] to study structural phase transitions in magnetic iron. SLD treats the dynamics of lattice and magnetic subsystems within a unified framework. Lattice and spin temperatures [51] can be well controlled through Langevin thermostats [34,52,53]. SLD also treats anharmonicity and coupling between lattice vibrations and magnetic excitations. SLD is an efficient and versatile simulation approach, and it has been recently applied to a variety of phenomena including anomalous self-diffusion in iron [54,55], magnetic excitations in thin films [56], and other magnetic phenomena [57–60].

To assess the relative stability of phases, it is necessary to compute the magnetic free energy, where the treatment of SRMO is critically important [22,38]. The SRMO is treated by SLD through the use of dynamic spin equations of motion. In this work, interatomic interaction parameters for SLD simulations are derived from *ab initio* calculations, and are given in the form of a noncollinear magnetic many-body potential. Using SLD simulations, we are able to evaluate contributions to the total free energy from lattice and spin excitations as functions of temperature. By a direct simulation, we find α-γ and γ-δ phase transitions, which correspond to changes of the sign of $\Delta F^{\text{fcc-bcc}}$. The maximum free energy difference between bcc and fcc phases over the temperature interval between the two phase transitions is close to 2 meV per atom.

II. FREE ENERGY CALCULATIONS

We calculate the Helmholtz free energy using the NVT ensemble. We use two complementary techniques to carry out free energy calculations, the umbrella sampling and adiabatic switching thermodynamic integration. Both methods are well established but they have not yet been applied to the treatment of phase transitions in magnetic systems. Brief summaries of the techniques are given below. We also evaluate the free energy of a harmonic oscillator and a Landau oscillator in the classical limit, and outline our sampling procedure.

Since we only treat the classical limit, our results are valid at temperatures that are sufficiently high, close to, or above, approximately one-third of a characteristic temperature of a particular subsystem, the Debye temperature for lattice vibrations and the Curie or the Néel temperature for magnetic excitations. Low-temperature classical results are only given for completeness, and they should not be treated as predictions. A quantum treatment, not considered below, should be applied if one is interested in the accurate low temperature values.

In the lattice case, the average number of phonons in mode k, $\langle n_k \rangle$, is given by the Planck distribution, where at sufficiently high temperatures

$$\langle n_k \rangle + \frac{1}{2} = \frac{1}{\exp\left(\frac{\hbar\omega_k}{k_B T}\right) - 1} + \frac{1}{2} \approx \frac{k_B T}{\hbar\omega_k} + \frac{1}{12}\left(\frac{\hbar\omega_k}{k_B T}\right) + \cdots .$$

Taking as an estimate $\hbar\omega_k \sim k_B T_D$, we see that the classical treatment applies at $T \geqslant T_D/\sqrt{12} \approx T_D/3.5$. The Debye temperature of iron is close to 470 K. Therefore we see that the temperature range of validity of classical molecular dynamics is defined by the condition $T > 135$ K [61]. A broadly similar argument can also be applied to magnetic excitations, which we treat classically at temperatures above approximately one third of T_C or T_N.

A. Umbrella sampling

Umbrella sampling [62] is a biased sampling technique. It is a re-weighting technique for evaluating the difference between free energies of a reference and a target state. It is particularly useful for sampling metastable states.

We start by considering two classical Hamiltonians $\mathcal{H}^0$ and $\mathcal{H}^1$, and their difference:

$$\delta\mathcal{H}_{um} = \mathcal{H}^1 - \mathcal{H}^0. \tag{1}$$

The ensemble average or, equivalently, the expectation value of an observable $\mathcal{O}$ in a configuration defined by Hamiltonian $\mathcal{H}^0$ at a particular temperature T is

$$\langle\mathcal{O}\rangle_0 = \frac{\int \mathcal{O}\exp(-\beta\mathcal{H}^0)d\Omega}{\int \exp(-\beta\mathcal{H}^0)d\Omega}, \tag{2}$$

where $\beta = (k_B T)^{-1}$ and $d\Omega$ is an element of volume in classical phase space, which in this instance has 9N dimensions, and includes position vectors of all the atoms, their kinematic momenta, and vectors of all the atomic magnetic moments. Substituting (1) into (2), we arrive at

$$\langle\mathcal{O}\rangle_0 = \frac{\langle\mathcal{O}\exp(\beta\delta\mathcal{H}_{um})\rangle_1}{\langle\exp(\beta\delta\mathcal{H}_{um})\rangle_1}. \tag{3}$$

This formula recasts the calculation of an ensemble average of a classic observable $\mathcal{O}$ over an equilibrium state defined by Hamiltonian $\mathcal{H}^0$ into calculations of ensemble averages of $\mathcal{O}\exp(\beta\delta\mathcal{H}_{um})$ and $\exp(\beta\delta\mathcal{H}_{um})$ over thermodynamic equilibrium defined by another Hamiltonian $\mathcal{H}^1$.

This shows a way of evaluating the difference between free energies associated with two classical Hamiltonians $\mathcal{H}^0$ and $\mathcal{H}^1$. For example, the free energy corresponding to Hamiltonian $\mathcal{H}^0$ can be written as

$$\begin{aligned}
F^0 &= -k_B T \ln \int \exp(-\beta\mathcal{H}^0)d\Omega \\
&= -k_B T \ln \int \exp(-\beta(\mathcal{H}^0 - \mathcal{H}^1 + \mathcal{H}^1)d\Omega \\
&= -k_B T \ln \int \exp(\beta\delta\mathcal{H}_{um} - \beta\mathcal{H}^1)d\Omega \\
&= -k_B T \ln \left\{ \left[\frac{\int \exp(\beta\delta\mathcal{H}_{um} - \beta\mathcal{H}^1)d\Omega}{\int \exp(-\beta\mathcal{H}^1)d\Omega} \right] \right. \\
&\quad \left. \times \int \exp(-\beta\mathcal{H}^1)d\Omega \right\} \\
&= -k_B T \ln\langle\exp(\beta\delta\mathcal{H}_{um})\rangle_1 + F^1.
\end{aligned} \tag{4}$$

Hence the difference between the free energies of two equilibrium configurations defined by Hamiltonians $\mathcal{H}^0$ and $\mathcal{H}^1$ equals

$$\begin{aligned}
\delta F_{um} &= F^1 - F^0 \\
&= k_B T \ln\langle\exp(\beta\delta\mathcal{H}_{um})\rangle_1.
\end{aligned} \tag{5}$$

If one of the free energies F^1 is known, the other free energy F^0 can be computed by sampling the phase space with thermodynamic weights defined by $\mathcal{H}^1$, and no independent averaging over thermodynamic equilibrium defined by $\mathcal{H}^0$ is required.

B. Adiabatic switching thermodynamic integration

Another technique for evaluating free energy differences is the adiabatic switching thermodynamic integration method [63–65]. It is a nonequilibrium technique that has superior efficiency as well as controlled systematic error in comparison with standard thermodynamic integration [66,67].

In a standard thermodynamic integration approach, for any two Hamiltonians $\mathcal{H}^0$ and $\mathcal{H}^1$, we can define a Hamiltonian that is a linear combination of the two, namely,

$$\mathcal{H}_{ti}(\lambda) = (1-\lambda)\mathcal{H}^0 + \lambda\mathcal{H}^1, \tag{6}$$

where λ is a switching parameter varying from 0 to 1. The difference between Hamiltonians $\mathcal{H}^1$ and $\mathcal{H}^0$ equals the derivative of $\mathcal{H}_{ti}$ with respect to λ:

$$\delta\mathcal{H}_{ti} = \mathcal{H}^1 - \mathcal{H}^0 = \frac{\partial\mathcal{H}_{ti}}{\partial\lambda}. \tag{7}$$

The free energy difference between the initial ($\lambda = 0$) and final ($\lambda = 1$) states can be calculated as an integral over the switching parameter, namely,

$$\delta F_{ti} = F^1 - F^0 = \int_0^1 \langle\delta\mathcal{H}_{ti}\rangle_\lambda d\lambda. \tag{8}$$

Brackets $\langle\cdots\rangle_\lambda$ correspond to taking an ensemble average with respect to $\mathcal{H}_{ti}(\lambda)$. The free energy difference equals the reversible work done by the thermodynamic driving force $\partial\mathcal{H}_{ti}/\partial\lambda$ along the transformation pathway.

In the adiabatic switching approach, this average is evaluated using a dynamic simulation, imposing the chain rule $d\lambda = (\partial\lambda/\partial t)dt$ and adopting a time-dependent switching function [68],

$$\lambda(\tau) = \tau^5(70\tau^4 - 315\tau^3 + 540\tau^2 - 420\tau + 126), \tag{9}$$

where $\tau = t/t_{\text{tot}}$, t is the elapsed time and t_{tot} is the total switching time. If $t = 0$ then $\lambda = 0$, and if $t = t_{\text{tot}}$ then $\lambda = 1$.

The free energy difference is estimated using a dynamic sequence of nonequilibrium states. One needs to be careful about the systematic error due to the irreversible nature of the nonequilibrium process, where heat dissipation is responsible for a part of the irreversible work done along the transformation pathway [67]. The above functional form gives rise to less dissipation during switching [66,68]. This point is explored in more detail in Appendix C.

C. Harmonic oscillator and Landau oscillator

We use two reference states in the free energy calculations. A harmonic oscillator is used as a reference state for the treatment of lattice vibrations. A Landau oscillator is used as a reference state for the treatment of magnetic excitations.

The Hamiltonian of a three-dimensional harmonic oscillator is

$$\mathcal{H}_{\text{HO}} = \frac{\mathbf{p}^2}{2m} + \frac{1}{2}m\omega^2\mathbf{x}^2 + C, \tag{10}$$

where $\mathbf{p}$ is the kinematic momentum, $\mathbf{x}$ is the displacement, ω is the frequency, m is the mass, and C is a constant. In the classical limit, the free energy can be evaluated analytically as

$$F_{\text{HO}} = -3k_B T \ln\left(\frac{k_B T}{\hbar\omega}\right) + C, \tag{11}$$

where the Planck constant is introduced for dimensional convenience. In what follows, we assume that ω equals the Debye frequency of iron, $\hbar\omega = k_B T_D$, where $T_D = 470$ K.

The Landau spin Hamiltonian has the form

$$\mathcal{H}_{\rm LO} = A_{\rm LO}\mathbf{S}^2 + B_{\rm LO}\mathbf{S}^4, \tag{12}$$

where $A_{\rm LO}$ and $B_{\rm LO}$ are constants, and $\mathbf{S}$ is a dimensionless spin vector. The free energy of magnetic excitations in the Landau approximation can be written as

$$F_{\rm LO} = -k_B T \ln\left(4\pi \int_0^\infty \exp(-\beta\mathcal{H}_{\rm LO}) S^2 dS\right), \tag{13}$$

where S is the magnitude of $\mathbf{S}$. In this work, we choose $A_{\rm LO} = -1.184$ eV and $B_{\rm LO} = 0.578$ eV to match the spectrum of longitudinal magnetic excitations [34]. The value of $F_{\rm LO}$ is computed numerically at various temperatures.

Hamiltonians $\mathcal{H}_{\rm HO}$ and $\mathcal{H}_{\rm LO}$ defined above refer to an individual atom and an individual spin. In the calculations below, we use $\mathcal{H}_{\rm HO}$ and $\mathcal{H}_{\rm LO}$ to represent all the atoms and spins, assuming that in the reference state they are independent of each other.

D. Sampling procedure: MD

In an MD simulation, the free energy is evaluated using the umbrella sampling. The full lattice Hamiltonian has the form

$$\mathcal{H}_l = \sum_i \frac{\mathbf{p}_i^2}{2m} + U(\mathbf{R}), \tag{14}$$

where $U(\mathbf{R})$ is the interatomic potential, $\mathbf{R} = \{\mathbf{R}_i\}$ are the coordinates of all the atoms, and $\mathbf{p} = \{\mathbf{p}_i\}$ are the kinematic momenta.

The free energy of the lattice system can be computed using Eq. (4) and sampling over the thermodynamic equilibrium of harmonic oscillators, namely,

$$F_l = F_{\rm HO} - \delta F_l, \tag{15}$$

where

$$\delta F_l = k_B T \ln\langle \exp(\beta\delta\mathcal{H}_l)\rangle_{\rm HO}, \tag{16}$$

and $\delta\mathcal{H}_l$ is defined as

$$\begin{aligned}\delta\mathcal{H}_l &= \mathcal{H}_{\rm HO} - \mathcal{H}_l \\ &= \sum_i \left(\frac{1}{2}m\omega^2\mathbf{x}_i^2 + C\right) - U(\mathbf{R}).\end{aligned} \tag{17}$$

Here, $\mathbf{x}_i$ is the displacement of atom i from its position in the lattice $\mathbf{R}_i^0$, i.e., $\mathbf{x}_i = \mathbf{R}_i - \mathbf{R}_i^0$. The value of constant C is chosen to minimize the variation of $\delta\mathcal{H}_l$. A suitable choice of C helps ensure the numerical stability of umbrella sampling by eliminating large numerical values in the argument of exponential function in Eq. (16). Technically, we find a suitable value of C by increasing or decreasing it, depending on the magnitude of $\delta\mathcal{H}_l$, during the thermalization process. Once thermalization is accomplished, we fix the value of C for the subsequent sampling. It is necessary to evaluate C in different situations because of the anharmonicity of interaction between the atoms at different temperatures and configurations.

Sampling is performed using dynamic Langevin thermostat simulations [52,53] that generate the correct equilibrium energy distribution, assuming ergodicity. Langevin equations of motion have the form

$$\begin{aligned}\frac{d\mathbf{R}_i}{dt} &= \frac{\mathbf{p}_i}{m}, \\ \frac{d\mathbf{p}_i}{dt} &= \mathbf{F}_i - \gamma_l\frac{\mathbf{p}_i}{m} + \mathbf{f}_i,\end{aligned} \tag{18}$$

where the regular component of the force acting on atom i is

$$\mathbf{F}_i = -\frac{\partial\mathcal{H}_{\rm HO}}{\partial\mathbf{R}_i}. \tag{19}$$

The damping constant γ_l and the fluctuating force $\mathbf{f}_i$ are related *via* the fluctuation-dissipation theorem [52,53], namely, $\langle f_{\alpha i}(t) f_{\beta j}(t')\rangle = 2k_B T\gamma_l\delta_{\alpha\beta}\delta_{ij}\delta(t-t')$, where indexes α and β refer to Cartesian coordinates x, y, and z. By following the above procedure, we sample over the thermodynamic equilibrium defined by the Einstein model for a solid, where lattice sites are ordered as a bcc or fcc lattice.

A major advantage of umbrella sampling is that it overcomes the difficulty associated with sampling the spectrum of excitations of an unstable or metastable structure. For example, the recently developed interatomic potentials for iron [40,41] predict a stable bcc phase. The fcc phase is unstable, but since sampling is performed over an equilibrium defined by suitably spatially ordered harmonic oscillators, the fact that the crystal structure is unstable has no effect on the stability of the numerical procedure.

Furthermore, umbrella sampling is a biased sampling method. It is efficient when the phase spaces of the reference and target states are similar, which is the case of harmonic oscillators and atomic motion driven by forces derived from a many-body potential. On the other hand, if one applies adiabatic switching from harmonic oscillators to many-body potential, a metastable crystal structure may experience structural instability at the end of the switching process, and cause failure in a calculation.

E. Sampling procedure: SLD

In a spin-lattice dynamic (SLD) simulation, we adopted a two-step approach to free energy calculations. We use umbrella sampling, followed by adiabatic switching. We write the spin-lattice Hamiltonian as a sum of the lattice and spin parts,

$$\mathcal{H}_{sl} = \mathcal{H}_l + \mathcal{H}_s, \tag{20}$$

where the spin part $\mathcal{H}_s = \mathcal{H}_s(\mathbf{R},\mathbf{S})$ depends on atomic coordinates $\mathbf{R}$ and atomic spin vectors $\mathbf{S} = \{\mathbf{S}_i\}$. Since we use different functional forms to represent the Hamiltonians, in what follows we discuss the choice of the specific functional forms adopted in simulations.

First, we apply the umbrella sampling. We define an auxiliary Hamiltonian,

$$\mathcal{H}_{{\rm HO},s} = \mathcal{H}_{\rm HO} + \mathcal{H}_s, \tag{21}$$

which is a sum of the harmonic oscillators Hamiltonian and the spin Hamiltonian. The difference between this Hamiltonian

and the exact Hamiltonian is

$$\delta\mathcal{H}_l = \mathcal{H}_{\mathrm{HO},s} - \mathcal{H}_{sl} \tag{22}$$

$$= \sum_i \left(\frac{1}{2}m\omega^2\mathbf{x}_i + C\right) - U(\mathbf{R}). \tag{23}$$

Notably, this expression is exactly the same as that investigated in connection with the pure MD analysis. Sampling can again be performed using Langevin thermostat simulations. Since we now also need to take into account magnetic fluctuations, the full set of equations now includes equations of motion for the spins [34]:

$$\frac{d\mathbf{S}_i}{dt} = \frac{1}{\hbar}[\mathbf{S}_i \times \mathbf{H}_i] + \gamma_s\mathbf{H}_i + \boldsymbol{\xi}_i, \tag{24}$$

where the damping constant γ_s and the stochastic spin force $\boldsymbol{\xi}_i$ are related *via* the fluctuation-dissipation theorem $\langle\xi_{\alpha i}(t)\xi_{\beta j}(t')\rangle = 2k_BT\gamma_s\delta_{\alpha\beta}\delta_{ij}\delta(t-t')$. The effective exchange field acting on spin i is

$$\mathbf{H}_i = -\frac{\partial\mathcal{H}_{\mathrm{HO},s}}{\partial\mathbf{S}_i}. \tag{25}$$

Forces acting on atoms in (18) now depend on the orientation of atomic spins,

$$\mathbf{F}_i = -\frac{\partial\mathcal{H}_{\mathrm{HO},s}}{\partial\mathbf{R}_i}. \tag{26}$$

Similarly to the MD case, we evaluate the difference between the free energies of an equilibrium configuration defined by the spin-lattice Hamiltonian, and a configuration defined by the auxiliary Hamiltonian

$$\delta F_l = F_{\mathrm{HO},s} - F_{sl} \tag{27}$$

$$= k_BT\ln\langle\exp(\beta\delta\mathcal{H}_l)\rangle_{\mathrm{HO},s}. \tag{28}$$

At the second step, we perform adiabatic switching. We define a reference Hamiltonian

$$\mathcal{H}_{\mathrm{HO,LO}} = \mathcal{H}_{\mathrm{HO}} + \mathcal{H}_{\mathrm{LO}}, \tag{29}$$

which is a sum of the harmonic oscillators Hamiltonian and the Landau Hamiltonian. The difference between the reference and the auxiliary Hamiltonians is

$$\delta\mathcal{H}_s = \mathcal{H}_{\mathrm{HO,LO}} - \mathcal{H}_{\mathrm{HO},s} \tag{30}$$

$$= \mathcal{H}_{\mathrm{LO}} - \mathcal{H}_s. \tag{31}$$

The Hamiltonian required for carrying out adiabatic switching can be written as

$$\mathcal{H}_{ti}(\lambda) = \mathcal{H}_{\mathrm{HO}} + (1-\lambda)\mathcal{H}_s + \lambda\mathcal{H}_{\mathrm{LO}}. \tag{32}$$

Langevin equations of motion remain unchanged, but the effective field and the force now depend on the integration parameter λ, namely,

$$\mathbf{H}_i = -\frac{\partial\mathcal{H}_{ti}(\lambda)}{\partial\mathbf{S}_i}, \tag{33}$$

$$\mathbf{F}_i = -\frac{\partial\mathcal{H}_{ti}(\lambda)}{\partial\mathbf{R}_i}. \tag{34}$$

The free energy difference between the equilibrium states defined by the auxiliary and reference Hamiltonians is

$$\delta F_s = F_{\mathrm{HO,LO}} - F_{\mathrm{HO},s} \tag{35}$$

$$= \int_0^1 \langle\delta\mathcal{H}_s\rangle_\lambda d\lambda. \tag{36}$$

Combining the results derived using the umbrella sampling and adiabatic switching, we find the free energy of the equilibrium configuration defined by the spin-lattice Hamiltonian

$$F_{sl} = F_{\mathrm{HO,LO}} - \delta F_l - \delta F_s. \tag{37}$$

We note that this free energy F_{sl} can be represented as a sum:

$$F_{sl} = F_l + F_s, \tag{38}$$

where

$$F_l = F_{\mathrm{HO}} - \delta F_l,$$
$$F_s = F_{\mathrm{LO}} - \delta F_s. \tag{39}$$

The above expression has a clear meaning, since F_l represents a part of the free energy associated primarily with lattice excitations, whereas F_s is a part of the free energy derived primarily from spin fluctuations. Since the spin and lattice degrees of freedom are coupled, and we sample through an auxiliary step, it would be inaccurate to interpret F_l and F_s as independent contributions from the lattice and spin subsystems. However, the two quantities still provide some qualitative insight into the relative magnitude of contributions by the two coupled subsystems to the total free energy.

The use of a two-step approach is essential for performing an accurate evaluation of the free energy of a spin-lattice system. As noted above, umbrella sampling overcomes the difficulty associated with sampling a metastable crystal structure. However, since the reference Hamiltonian of the spin subsystem is a set of Landau oscillators corresponding to noninteracting magnetic moments, its phase space does not resemble a system of interacting magnetic moments, especially in the limit of low temperatures where magnetic moment-moment correlations are strong. Even at temperatures higher than the Curie temperature, the moment-moment correlations do not vanish [50]. In principle, the umbrella sampling method can tackle this issue through extensive sampling, but it is more computationally expedient to use adiabatic switching when calculating the free energy difference between the spin states.

The choice of an auxiliary Hamiltonian is nontrivial. If we choose $\mathcal{H}_{l,\mathrm{LO}} = \mathcal{H}_l + \mathcal{H}_{\mathrm{LO}}$ as the auxiliary Hamiltonian, when we perform adiabatic switching to calculate the free energy difference between $\mathcal{H}_{sl}$ and $\mathcal{H}_{l,\mathrm{LO}}$, the lattice subsystem may experience instability during the calculation. The current choice of the auxiliary Hamiltonian $\mathcal{H}_{\mathrm{HO},s}$ allows us to apply umbrella sampling to the lattice subsystem and adiabatic switching to the spin subsystem. It ensures the stability of crystal lattice and computational efficiency of the free energy calculations.

III. SIMULATIONS PERFORMED USING PUBLISHED SETS OF PARAMETERS

Using the methods described above, we performed MD and SLD simulations, using parameters taken from literature. All the simulations were performed using our MD and SLD program SPILADY [69]. We used cubic simulation cells containing 16000 atoms in the bcc case and 16384 atoms in the fcc case. We explored temperatures in the range from 1 K to 1400 K. For each temperature, we simulated samples at nine different volumes, close to an assumed equilibrium volume. A third-order polynomial was then fitted to the calculated free energies. The equilibrium volume was determined from the minimum of the polynomial. All the values given below are the interpolations corresponding to the equilibrium volume. The initial, guessed, equilibrium volume was estimated using the same approach, starting from a larger interval of trial volumes.

In Fig. 1, the free energy, computed using SLD simulations, is plotted as a function of volume for bcc crystal structure at $T = 300$ and 1000 K. The polynomial fit interpolates between the data points fairly well, although fluctuations are larger at higher temperatures, affecting the accuracy of evaluation of the equilibrium lattice constant. The dotted blue curves show the standard deviation computed for the fitted curve, shown in red. Standard deviation is evaluated using the covariance matrix of coefficients of the polynomial. The position of the free energy minimum remains accurate at the sub-meV accuracy level, as illustrated by the scale of the y axis.

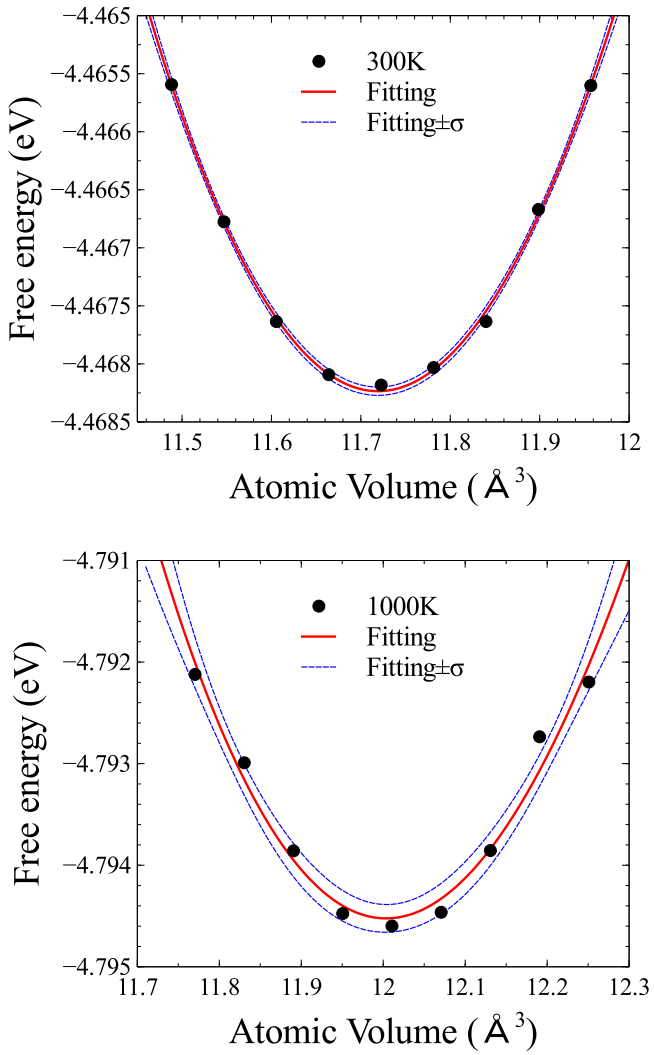

FIG. 1. Free energies of bcc iron computed using spin-lattice dynamics for $T = 300$ and 1000 K as functions of volume. The fitted curve shown in red is a third-order polynomial. The dotted curves shown in blue illustrate the standard deviation of the fitted curve, shown in red.

All the simulation cells were thermalized to equilibrium before sampling. In MD, 100 000 data points are used for umbrella sampling. In SLD, 200 000 data points are used in umbrella sampling, and the total switching time in adiabatic switching is 0.2 ns. The Marinica iron potential [40,41] is used in MD and SLD simulations. SLD simulations are based on the spin Hamiltonian of the form [34,50]:

$$\mathcal{H}_s = -\frac{1}{2}\sum_{i,j} J_{ij}(R_{ij})(\mathbf{S}_i \cdot \mathbf{S}_j - |\mathbf{S}_i||\mathbf{S}_j|) + \sum_i \left(A_i \mathbf{S}_i^2 + B_i \mathbf{S}_i^4\right), \quad (40)$$

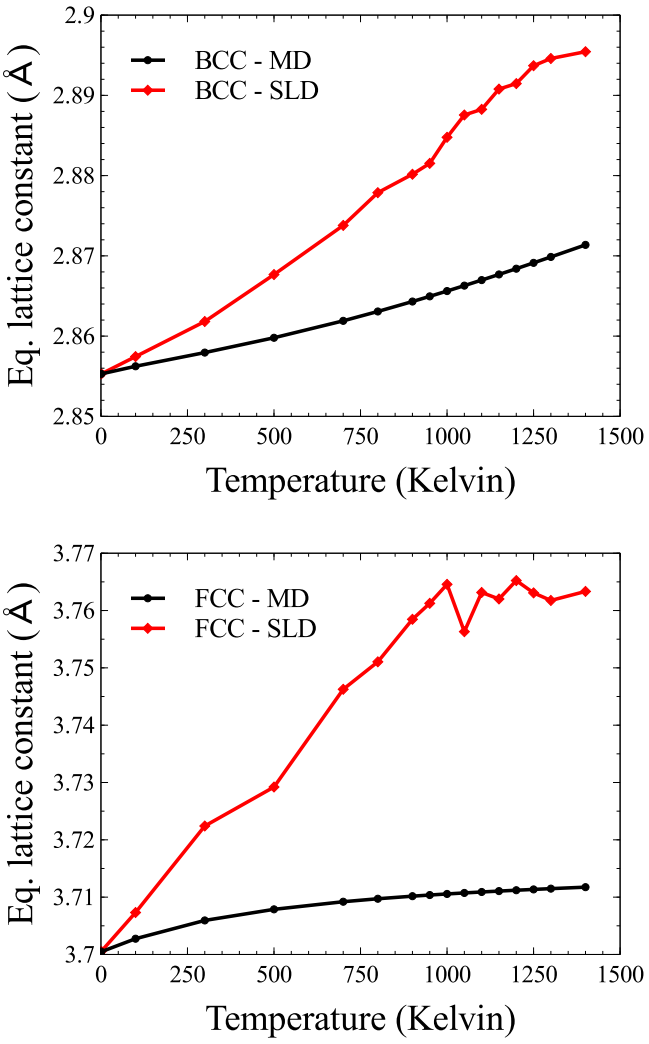

FIG. 2. Equilibrium lattice constants of bcc and fcc phases as functions of temperature, computed using MD and SLD simulations.

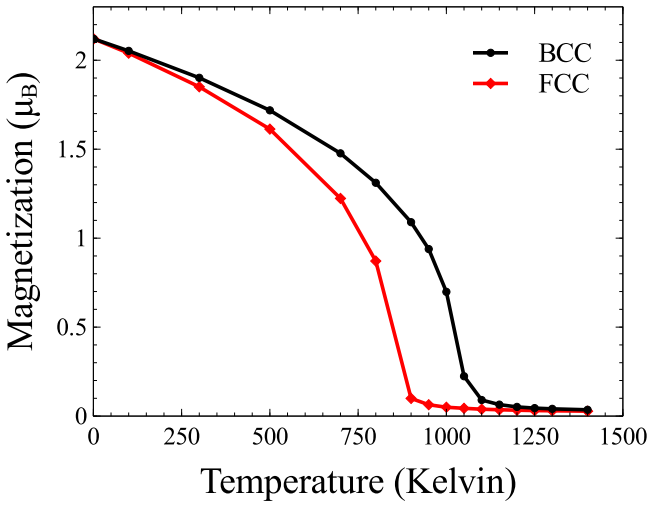

FIG. 3. Magnetization as a function of temperature, computed using SLD simulations.

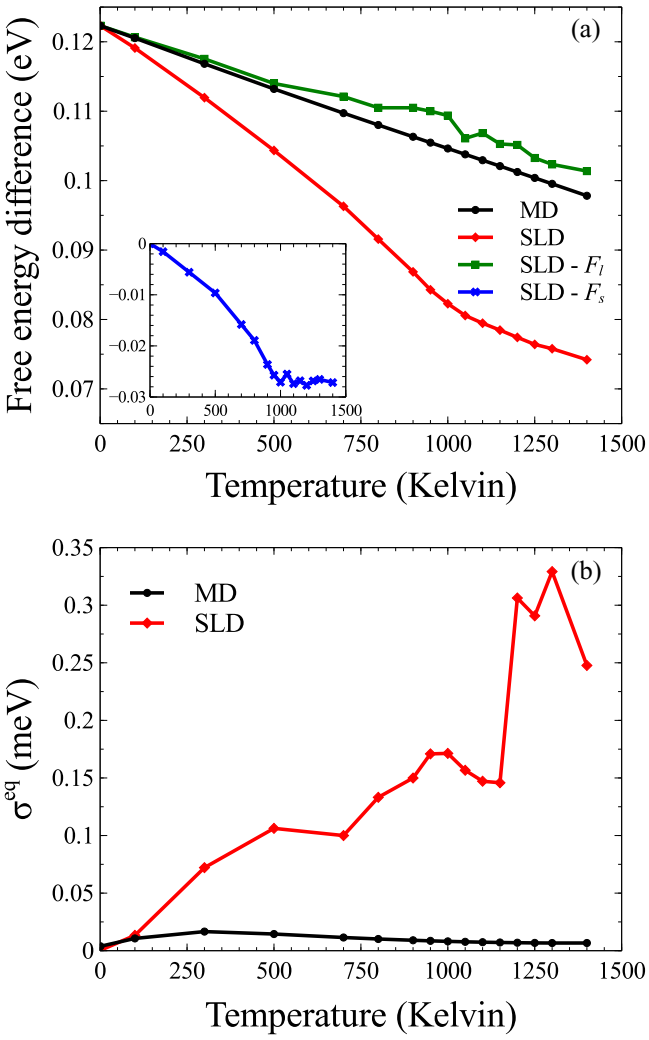

FIG. 4. (a) Difference between the free energies of fcc and bcc phases plotted as a function of temperature. Data derived from MD and SLD are shown, with lattice and spin contributions shown separately. (b) Standard deviation of the free energy, computed assuming the equilibrium value of the lattice constant.

where J_{ij} is the exchange coupling function, and A_i and B_i are the Landau coefficients for atom i. The form of H_s guarantees that the energy difference between bcc and fcc structures at 0 K is the same as in a calculation performed using a nonmagnetic MD potential.

We assume that J_{ij} is a pairwise function depending only on the distance between atoms i and j. It has the form $J_{ij}(r) = J_0(1 - r/r_c)^3\Theta(r_c - r)$, where $J_0 = 0.92$ eV and $r_c = 3.75$ Å. The value of J_0 is slightly larger than the one derived in Ref. [50] to match the experimental value of the Curie temperature T_C. Parameters $A_i = -0.744824$ eV and $B_i = 0.345295$ eV are the same as in Ref. [34]. We note that the ground state of this Hamiltonian is ferromagnetic regardless of whether the underlying crystal structure is bcc or fcc.

Figure 2 shows equilibrium lattice constants as functions of temperature, predicted by MD and SLD simulations. Magnetic excitations enhance thermal expansion of both bcc and fcc structures. The curves derived from SLD simulations flatten in the vicinity of T_C (Fig. 3). Fluctuation of the curves result primarily from polynomial fitting.

Since the same spin Hamiltonian is used in bcc and fcc cases, they both adopt ferromagnetic ground states at temperatures below T_C. However, experimental data for fcc iron indicate that it has a relatively low Néel temperature T_N of 67 K [70,71]. Although the precise nature of magnetic configuration at temperatures below T_N is debatable, the net magnetization is zero. This differs from our simulations, and we will address the issue in the following sections.

In Fig. 4, we plotted the free energy difference between fcc and bcc phases as a function of temperature. We define the free energy difference as $\Delta F^{\text{fcc-bcc}} = F^{\text{fcc}} - F^{\text{bcc}}$. If this value is positive, bcc phase is stable and vice versa. In MD, $\Delta F^{\text{fcc-bcc}}$ is always positive and does not approach zero even if temperature increases. If we include magnetic excitations, $\Delta F^{\text{fcc-bcc}}$ decreases significantly. We show $\Delta F_l^{\text{fcc-bcc}} = F_l^{\text{fcc}} - F_l^{\text{bcc}}$ on the same graph, and $\Delta F_s^{\text{fcc-bcc}} = F_s^{\text{fcc}} - F_s^{\text{bcc}}$ in the inset. The free energy difference predicted by SLD simulations largely originates from the spin subsystem, though it is not sufficient to stabilize the fcc phase at high temperature. We also note that the derivative of $\Delta F_s^{\text{fcc-bcc}}$ with respect to temperature is small near the Curie temperature T_C of the bcc phase. Standard deviations of the calculated free energies are also shown, they are all in the sub-meV range.

Although we find that the magnetic part of the free energy is fairly large, we see that simulations that use parameters taken from literature have no chance of success in predicting the bcc-fcc phase transition. The main deficiency of the existing parametrizations is that all the interatomic potentials were fitted without considering magnetic excitations. Even if we add a spin part to the Hamiltonian in an *ad hoc* manner, this still does not fully account for the free energy contribution from the spin system. A better approach to deriving parameters for spin-lattice dynamics simulations needs to be developed and applied, to model magnetic iron on the atomic scale.

IV. PARAMETRIZATION

In what follows, we present a new derivation of parameters for spin-lattice dynamics simulations of bcc and fcc iron. We start by fitting a nonmagnetic iron potential, and augment it by the Heisenberg-Landau Hamiltonian.

A. Nonmagnetic iron potential

We fit a nonmagnetic iron potential using an interatomic potential fitting program *potfit* [72–74]. It fits a many-body potential to a user-defined functional form. Parameters of the potential are fitted using the force matching method [75], using the total energy and forces taken from *ab initio* data. All of our *ab initio* calculations were performed using Vienna *Ab initio* simulation package (VASP) [76–79] with projector augmented wave (PAW) potentials. We use GGA-PBE [80,81] pseudopotential with 14 valence electrons. The plane-wave energy cutoff is 450 eV.

We first generate *ab initio* data for nonmagnetic iron. The structures include perfect bcc and fcc lattices, and simulation cells with rhombohedral and tetragonal distortions, at various volumes. We also produce *ab initio* data for amorphous structures, and structures containing defects. The size of simulation cells and number of atoms in each cell depend on the fitting requirements. The functional form and parameters of the fitted potential are given in Appendix. Since we are only interested in energy and free energy differences between bcc and fcc structures, we do not discuss other features of our nonmagnetic iron potential here.

Figure 5 shows *ab initio* energies of nonmagnetic bcc and fcc phases at various lattice constants. The minimum energy of the fcc phase is 0.312 eV lower than the minimum energy of the bcc phase, in agreement with data from Ref. [5]. Fcc structure is more stable when magnetism is not taken into account. The curves computed using nonmagnetic potential appear similar, and the energy difference is 0.317 eV. The difference between the absolute values of *ab initio* data and nonmagnetic potential data is due to different reference points. Since we take the cutoff distance of the potential as 5.3 Å, energies of all the *ab initio* data points are reduced by the energy of a perfect bcc structure with lattice constant $a = 5.3\times 2/\sqrt{3} = 6.1199$ Å, where the nearest-neighbor distance is 5.3 Å. Interatomic forces remain unaffected by this procedure.

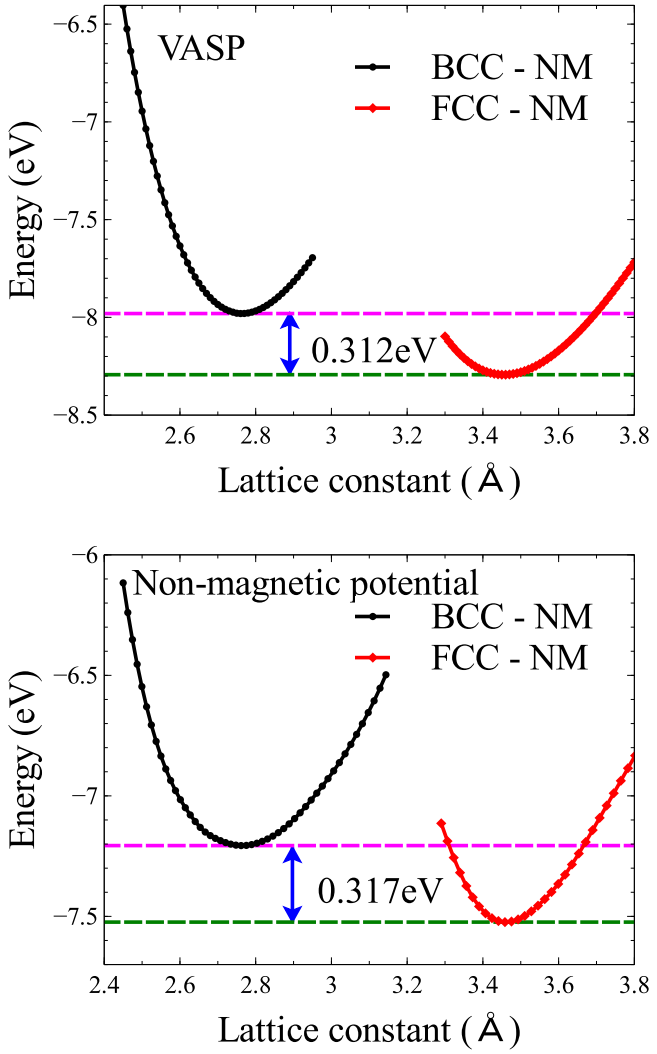

FIG. 5. Energy per atom computed for nonmagnetic bcc and fcc structures using VASP and the fitted nonmagnetic interatomic potential.

B. Magnetic contributions

Figure 6 shows VASP data for the energies of magnetic bcc and fcc phases at various lattice constants. In the bcc case, we only show the data for the FM collinear ground state. In the fcc case, there are a number of magnetic configurations that all have comparable energies. We show *ab initio* data for the FM, AFM, and double layer AFM (DLAFM) magnetic configurations. We used one atom in the calculation of bcc-FM case, one atom in fcc-FM case, four atoms in fcc-AFM case, and eight atoms in fcc-DLAFM case. If we impose a constraint and consider only collinear magnetic configurations,

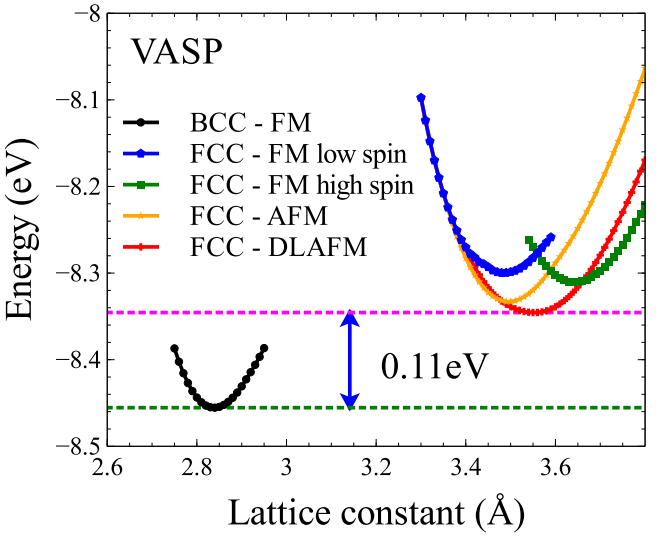

FIG. 6. Energies of ferromagnetic bcc, ferromagnetic (high spin and low spin) fcc, single layer antiferromagnetic fcc, and double layer antiferromagnetic fcc structures calculated using VASP.

the DLAFM state has the lowest energy. This also agrees with *ab initio* results given in Ref. [5].

The energy of the FM bcc phase is now 0.11 eV lower than that of the DLAFM fcc phase. We now need to find a way of describing magnetic excitations using a magnetic Hamiltonian added to the nonmagnetic Hamiltonian. This magnetic Hamiltonian should also describe interactions between magnetic moments that are not explicitly evident in the VASP data.

There are various ways of describing interactions between magnetic moments. One can use the spin spiral method [82] or spin-cluster expansion method [83]. We choose the spin Hamiltonian in the Heisenberg-Landau form [3,4,34],

$$\mathcal{H}_s = -\frac{1}{2}\sum_{i,j} J_{ij}(R_{ij})\mathbf{M}_i \cdot \mathbf{M}_j + \sum_i \left(A(\rho_i)\mathbf{M}_i^2 + B(\rho_i)\mathbf{M}_i^4\right), \quad (41)$$

where $\mathbf{M} = -g\mu_B \mathbf{S}_i$ is the magnetic moment of atom i, $g = 2.0023$ is the electron g factor, μ_B is the Bohr magneton, $A(\rho_i)$ and $B(\rho_i)$ are the Landau coefficients that depend on the effective electron density ρ_i. This is the same ρ_i that enters the nonmagnetic interatomic potential.

The first step is to calculate values of J_{ij} from the lowest energy state of bcc and fcc phases. The exchange coupling functions are calculated using *ab initio* electronic structure multiple-scattering formalism. We use the method and the program developed by van Schilfgaarde *et al.* [84,85]. It is based on the linear muffin-tin orbital approximation combined with Green's function technique (LMTO-GF). We calculated values of parameters J_{ij} involving various neighbours over a range of variation of the lattice constant. Figure 7 shows the calculated values and the fitted curves. *Ab initio* data for the bcc case are smoother, whereas the data for the fcc cases are more scattered. A possible reason is that magnetic configuration of the collinear FM state in bcc phase is fundamentally simpler than the DLAFM state of the fcc phase. To match the data, we used different functional forms for the bcc and fcc cases. The functional forms and values of parameters are given in Appendix.

We now can extract the Landau coefficients from the VASP data. We define a temporary Hamiltonian with no magnetic moment interactions, assuming that on-site magnetic moments can be treated as order parameters, i.e.,

$$\mathcal{H}'_s = \sum_i \left(A'\mathbf{M}_i^2 + B'\mathbf{M}_i^4\right). \quad (42)$$

Since we know the difference between energies of magnetic and nonmagnetic configurations (Fig. 8), and also the magnitude of magnetic moments on each atoms (Fig. 9) as functions of the lattice constant, we can identify the energy difference between magnetic and nonmagnetic states per atom as

$$\Delta E = A' M_0^2 + B' M_0^4. \quad (43)$$

M_0 is found by solving equation $\partial \Delta E / \partial M_0 = 0$, i.e.,

$$M_0 = \sqrt{-A'/2B'} \neq 0, \quad (44)$$

or $M_0 = 0$ if the nonmagnetic state is more stable. We find values of A' and B' at various lattice constants by solving the above equations.

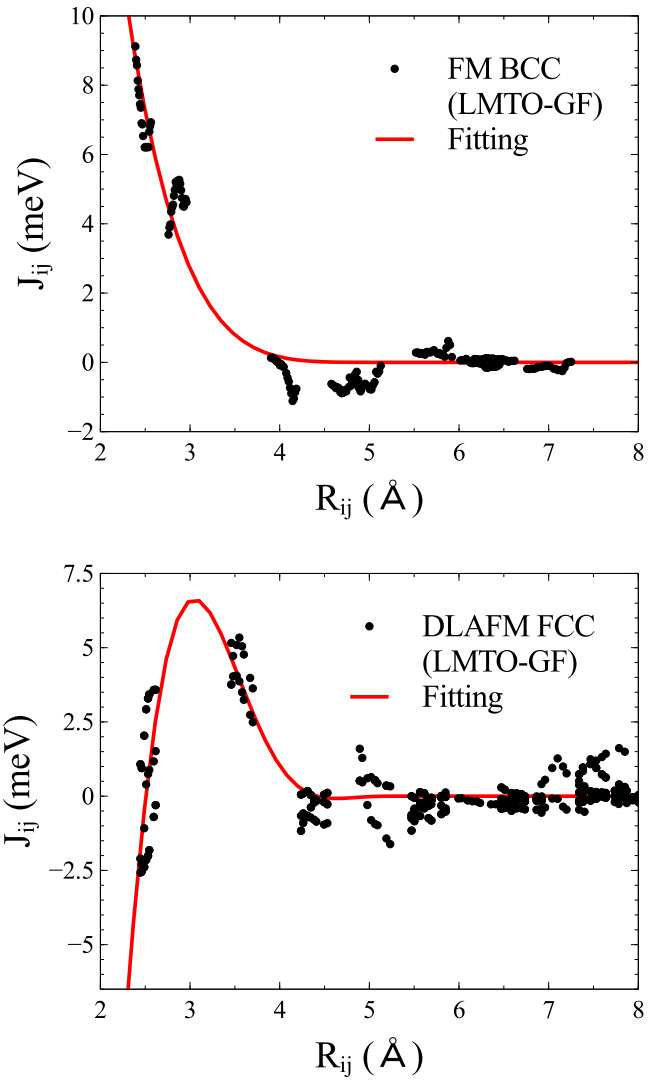

FIG. 7. Exchange coupling J_{ij} for the ferromagnetic bcc and double layers antiferromagnetic fcc structures calculated using the LMTO-GF method, and the fitting functions.

We now relate the values of Landau parameters to the values of parameters of the Hamiltonian describing interacting magnetic moments. We equate Eqs. (41) and (42) and find

$$A\mathbf{M}_i^2 = A'\mathbf{M}_i^2 + \frac{1}{2}\sum_j J_{ij}\mathbf{M}_i \cdot \mathbf{M}_j, \quad (45)$$

$$B = B'. \quad (46)$$

Using the fitted function J_{ij} and considering magnetic configurations of perfect crystals in bcc-FM case and fcc-DLAFM case, we find the values of Landau coefficients A and B for bcc and fcc at various volumes. Since fluctuations of atomic magnetic moments reflect fluctuations of local electron density, it is natural to assume that Landau coefficients are functions of the effective electron density ρ_i, which is a local quantity, defining also the local many-body potential.

These coefficients are plotted as functions of the effective electron density ρ_i for perfect crystals (Figs. 10 and 11). Again, we use different functional forms for fitting data for bcc and

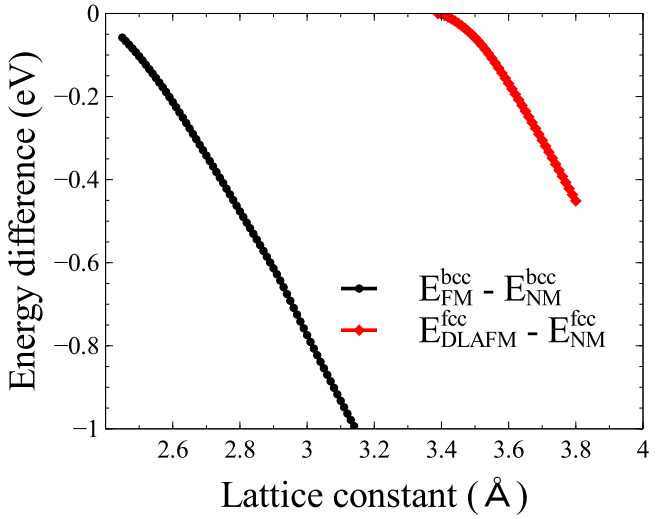

FIG. 8. Difference between energies of magnetic and nonmagnetic states of ferromagnetic bcc and double layers antiferromangetic fcc structures. Data are extracted from simulations illustrated in Fig. 6.

fcc cases, to match various features of the curves. Functional forms and numerical parameters are given in Appendix. Strong scatter of values for $B(\rho_i)$ is due to the small value of M_0 corresponding to small simulation cell size. We see that there is a sharp drop of magnetic moment in the fcc-DLAFM case in Fig. 9 if the lattice constant is less than 3.5 Å. This is responsible for the variation of B shown in Fig. 11 in the range $\rho_i > 7\ \mathrm{eV}^2$.

Using the above procedure, we generated several sets of parameters, which were all derived using different methods and have different functional forms. The set of parameters that has been selected for final simulations is the one that matches experimental results particularly well. Although all the parameters generate qualitatively similar predictions, Landau coefficients may need to be adjusted through the choice

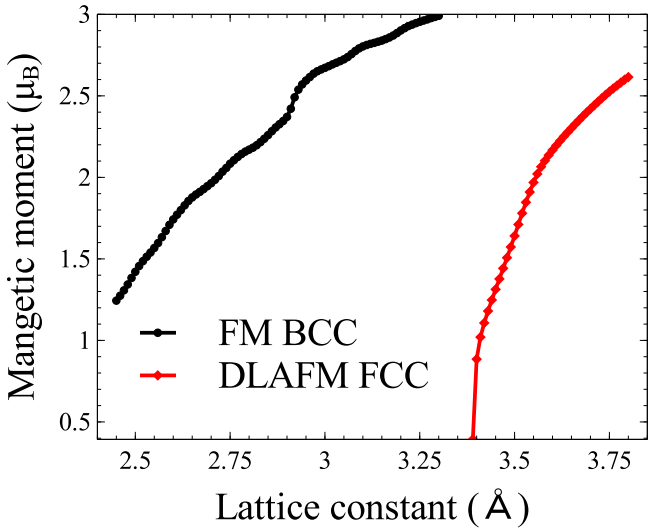

FIG. 9. Magnitude of magnetic moments computed for ferromagnetic bcc and double layers antiferromangetic fcc structures. Data are extracted from the simulations illustrated in Fig. 6.

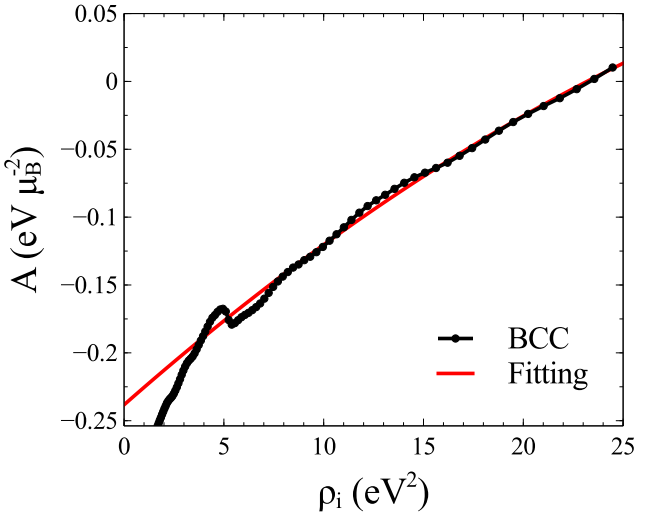

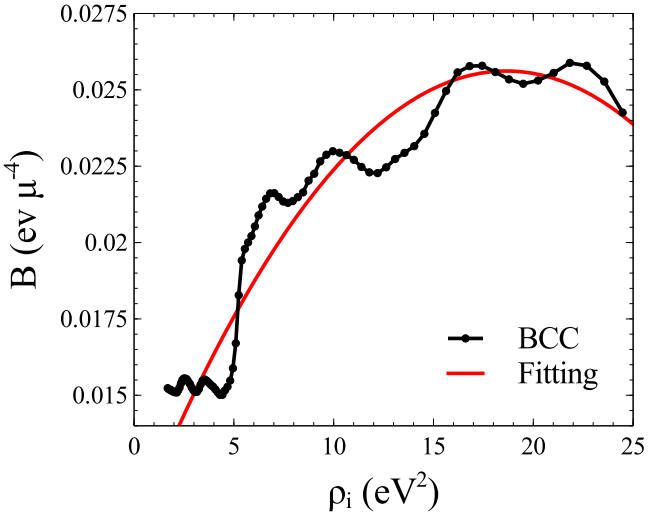

FIG. 10. Landau coefficients A and B as functions of the effective electron density ρ for bcc structures. They are computed using LMTO-GF and VASP data and the procedure described in the text. Red lines are fitted curves parameterized using values given in Appendix. They are also used in spin-lattice dynamic simulations.

of fitting intervals to achieve sub-meV accuracy of free energy calculations. In all the cases, *ab initio* data provide input for the fitting procedure.

In effect, in our approach, we follow the same strategy as the one used in fitting many-body potentials. The functional form and numerical parameters of a many-body potential are usually chosen to represent actual physical properties of a material, the data derived from experimental observations and *ab initio* calculations. There is no universal potential suitable for treating all the situations and all the physical properties. There is no universal scheme for many-body potential fitting either. Authors of many-body potentials often add their own features to potentials, depending on their understanding of physical properties and the physical problems that they intend to address. Our potentials are generated bearing in mind their application to modeling α-γ-δ phase transitions of magnetic iron.

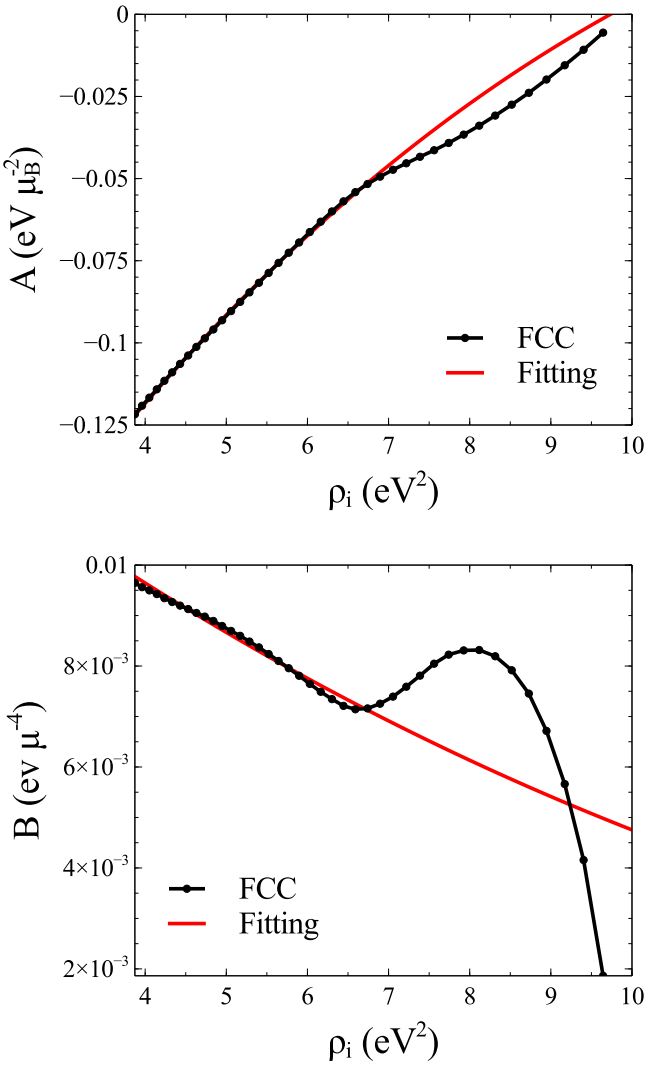

FIG. 11. Landau coefficients A and B as functions of the effective electron density ρ for fcc structures. They are computed using LMTO-GF and VASP data and the procedure described in the text. Red lines are fitted curves parameterized using values given in Appendix. They are also used in spin-lattice dynamic simulations.

V. STRUCTURAL PHASE TRANSITIONS

We calculated the free energies of bcc and fcc phases using the above new sets of parameters. We performed both MD and SLD simulations. In MD, we used the nonmagnetic potential, and performed umbrella sampling calculations using 100 000 data points. In SLD, we used the nonmagnetic potential in combination with the Heisenberg-Landau Hamiltonian, and used the two step approach in free energy calculations. We used 300 000 data points when performing the umbrella sampling, and 0.2 ns as the total switching time in the adiabatic switching procedure. Magnetic configurations of bcc and fcc lattices were initialized to FM and DLAFM states, respectively. We explored a large temperature interval from 1×10^{-5} to 2000 K. All that samples were thermalized to equilibrium before sampling.

The most significant results of this paper are illustrated in Figs. 12 and 13. Figure 12 shows the calculated free energies

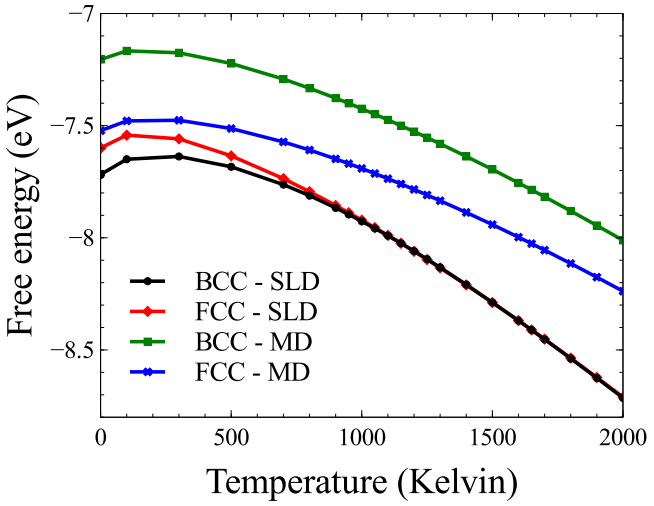

FIG. 12. Free energy of bcc and fcc phases as functions of temperature. Both MD and SLD results are shown.

of bcc and fcc phases at the equilibrium volume. In the MD case, the free energy of the fcc phase is always lower than the free energy of the bcc phase. In SLD, the bcc phase has lower free energy at low temperature, but the curves corresponding to bcc and fcc phases approach each other at higher temperature. There are two intersections between the curves, which can be seen if one follows the difference $\Delta F^{\text{fcc-bcc}}$ plotted in Fig. 13. The curve cross the zero line at around 1130 and 1600 K. These temperatures are close to the experimentally observed values of α-γ and γ-δ phase transitions, which occur in experiment at $T_{\alpha\text{-}\gamma} = 1185$ K and $T_{\gamma\text{-}\delta} = 1667$ K, respectively. The free energy difference at the minimum is close to 2 meV. This value agrees with the MCE [3,4] and RPA [11] results, and shows that α-γ-δ transitions are associated with fairly small

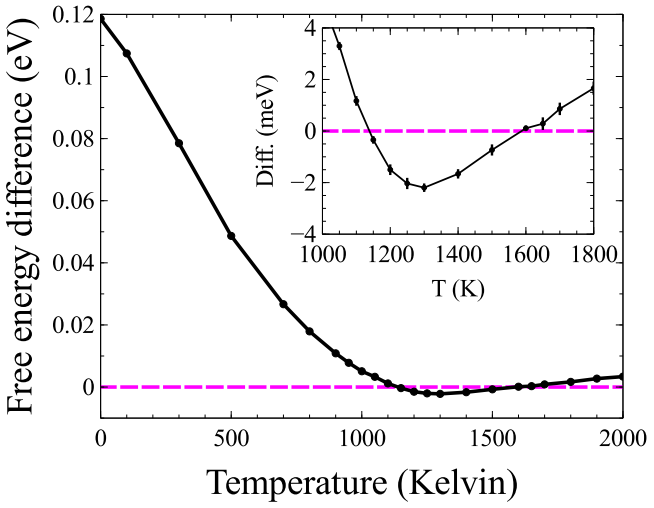

FIG. 13. Difference between free energies of bcc and fcc phases plotted as a function of temperature, with magnetic excitations and lattice vibrations contributions included. Calculations were performed using a nonmagnetic potential augmented with the Heisenberg-Landau Hamiltonian. The inset shows a magnified part of the same figure.

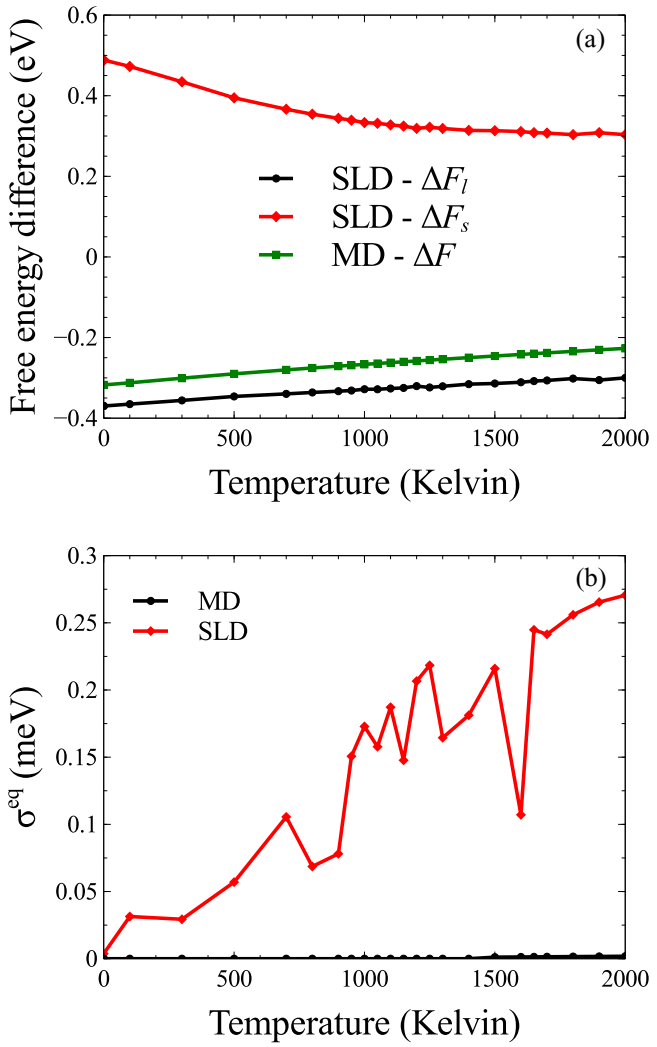

FIG. 14. (a) Lattice and spin contributions to the free energy difference between bcc and fcc phases. (b) Standard deviation of the free energy at the equilibrium lattice constant.

free energy differences between the competing phases, of the order of 1 meV.

The reason for the difference between MD and SLD simulations may be understood by considering free energy contributions from magnetic excitations and lattice vibrations. Figure 14 shows plots of $\Delta F_l^{\text{fcc-bcc}}$ and $\Delta F_s^{\text{fcc-bcc}}$ as functions of temperature. For comparison, we also plotted $\Delta F_{\text{MD}}^{\text{fcc-bcc}}$ calculated using the nonmagnetic potential. The value of $\Delta F_l^{\text{fcc-bcc}}$ is similar to $\Delta F_{\text{MD}}^{\text{fcc-bcc}}$. Both of them increase nearly linear as functions of temperature. On the other hand, $\Delta F_s^{\text{fcc-bcc}}$ decreases initially, but then flattens out near the Curie temperature T_C of the bcc phase. Hence the change of $\Delta F_s^{\text{fcc-bcc}}$ is mainly due to the degree of disorder associated with magnetic configurations involved. At temperatures above T_C, bcc phase is in a paramagnetic state, where long range magnetic order vanishes. Magnetic configurations of fcc and bcc phases are similar, making the entropy difference smaller. This interpretation is consistent with recent experimental observations [2] of phonon dispersion of iron. Experimental data suggest that

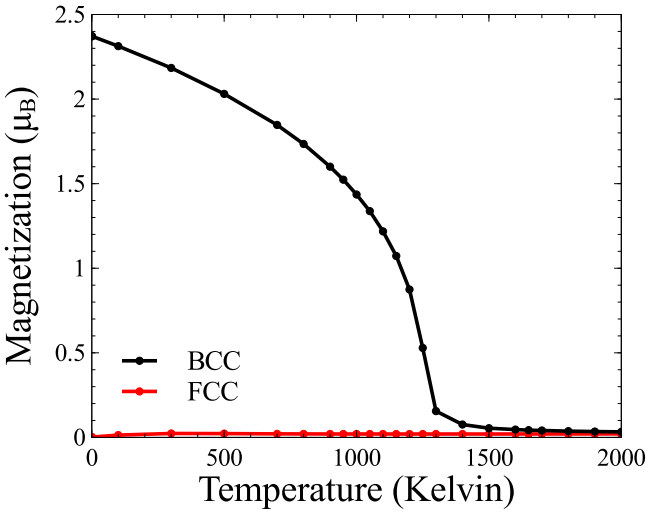

FIG. 15. Magnetization as a function of temperature computed using SLD simulations and the nonmagnetic potential augmented with the Heisenberg-Landau Hamiltonian.

the γ phase forms as a result of interplay between electronic (magnetic) and vibrational contributions to entropy, whereas the δ phase is stabilized primarily by vibrational entropy. The two crossing points result from the interplay between free energy contributions derived from the lattice and spin excitations. The standard deviation of the free energy remains in the sub-meV range.

The magnetization curve of iron is plotted in Fig. 15. For the bcc phase, the existing model predicts a relatively high Curie temperature at around 1300 K. For the fcc case, the predicted magnetization is zero. We investigated the Néel temperature T_N of the fcc phase by changing the value of energy per atom as a function of temperature (Fig. 16). We thermalized two simulation cells to 165 and 205 K. Then, we gradually increased the temperature of the simulation cell, equilibrated at 165 K, to 205 K. This was performed by increasing the thermostat temperature linearly over the time interval of 4 ns. Then, we decreased the temperature of the simulation cell, equilibrated at 205 K, back to 165 K. We filtered the output data by averaging over every thousand data points. We see that the magnetic subsystem undergoes a first-order transition at around 185 K. A jump of about 0.01 eV in the magnetic energy is observed. The change of the total energy is fully accounted for by the magnetic energy. The calculated T_N is higher than the experimental value of 67 K. However, such value is obtained from experiments on small particles [70,71] where the role of local stresses is uncertain. Besides, the temperatures of the α-γ and γ-δ phase transitions are significantly higher than T_N.

We also show the values of equilibrium lattice constants of bcc and fcc phases predicted by MD and SLD simulations in Fig. 17. The addition of the spin Hamiltonian changes the value of the equilibrium lattice constant even at 0 K. Fundamentally, this agrees with *ab initio* data shown in Figs. 5 and 6. The spin subsystem of the material affects mechanic properties through its contribution to the total free energy.

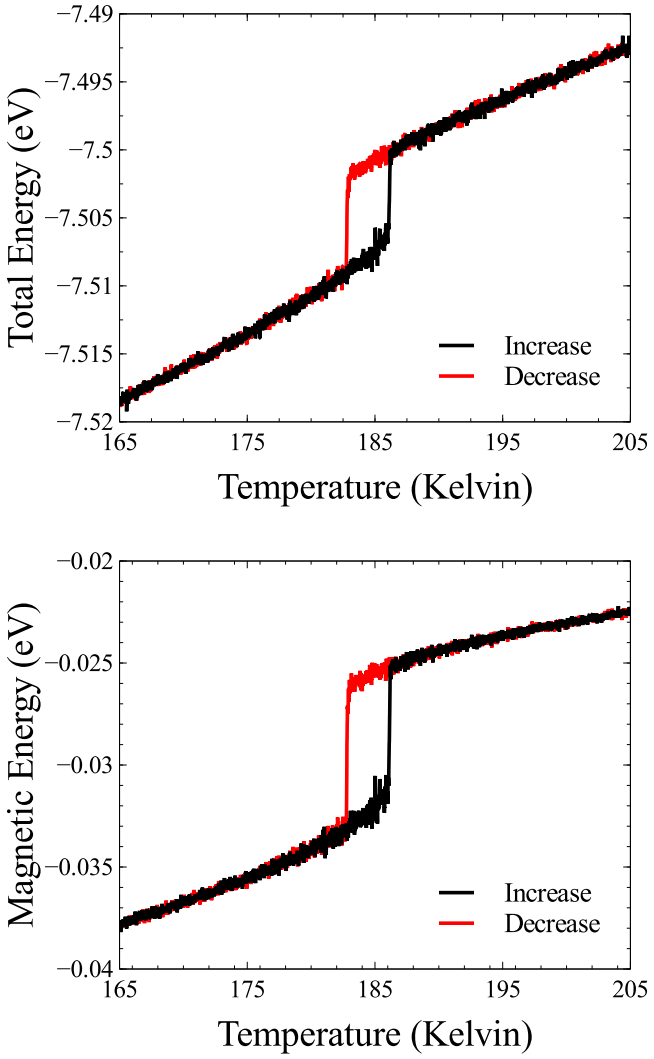

FIG. 16. The total energy and magnetic energy per atom as functions of temperature calculated by gradually increasing and decreasing the temperature of the thermostat.

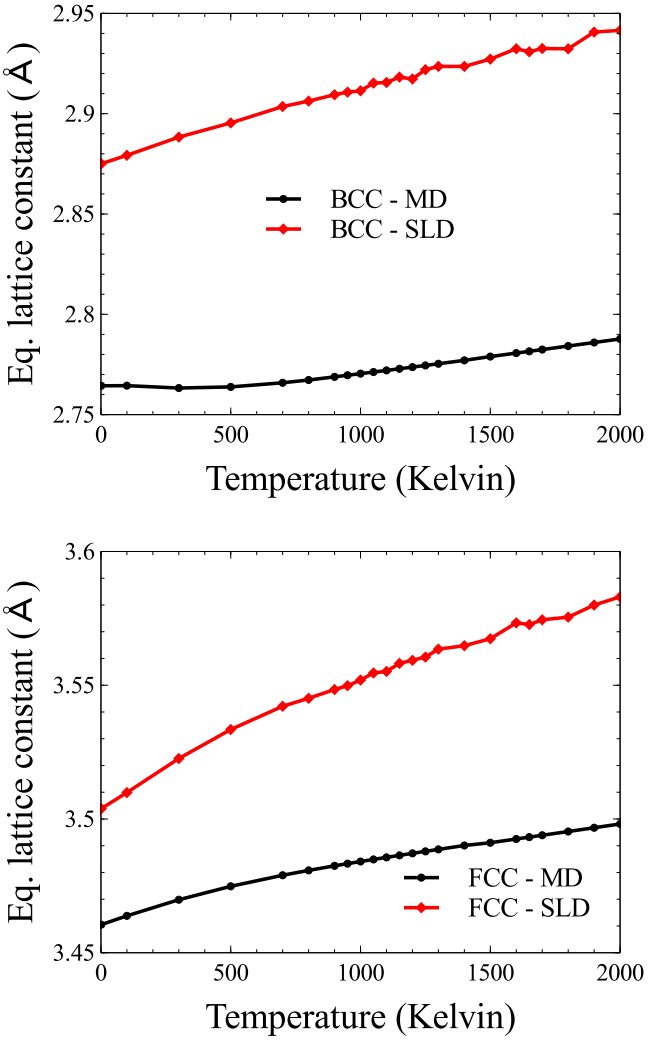

FIG. 17. Equilibrium lattice constants of bcc and fcc phases as functions of temperature, computed using MD and SLD simulations using the new interatomic potentials.

VI. CONCLUSIONS

Starting from a large amount of *ab initio* data, we fitted nonmagnetic many-body potentials and Heisenberg-Landau Hamiltonians for bcc and fcc iron. We performed free energy calculations using umbrella sampling and adiabatic switching thermodynamics integration. The free energy has been sampled by molecular dynamics and spin-lattice dynamics simulations. Our method provides a reasonably consistent way of assessing the phase stability of magnetic iron within a unified dynamic picture. It treats magnetic excitations and lattice vibrations and their coupling in a self-consistent way. The bcc-fcc (α-γ) and fcc-bcc (γ-δ) phase transitions in magnetic iron are reproduced using a newly fitted interatomic potential. The structural phase stability of magnetic iron is shown to be determined by a combined effect of noncollinear magnetic excitations and lattice vibrations, in agreement with several experimental and theoretical studies. The maximum free energy difference between bcc and fcc phases in the range of stability of fcc γ phase is approximately 2 meV per atom.

ACKNOWLEDGMENTS

This work has been carried out within the framework of the EUROfusion Consortium and has received funding from the Euratom research and training programme 2014-2018 under Grant agreement No. 633053 and from the RCUK Energy Programme [Grant No. EP/P012450/1]. To obtain further information on the data and models underlying this paper please contact PublicationsManager@ukaea.uk. The views and opinions expressed herein do not necessarily reflect those of the European Commission. We also acknowledge EUROFusion for the provision of access to Marconi supercomputer facility at CINECA in Italy. The authors are grateful to M.-C. Marinica for stimulating discussions.

APPENDIX A: NONMAGNETIC IRON POTENTIAL

The functional form of the interatomic potential broadly follows the conventional embedded atom method (EAM)

representation

$$U(\mathbf{R}_1,\mathbf{R}_2,\ldots)=\sum_i F(\rho_i)+\frac{1}{2}\sum_{i,j}V_{ij}(R_{ij}), \tag{A1}$$

where $\mathbf{R}_i$ is the position of atom i, ρ_i is the effective electron density and V_{ij} is a pairwise function that depends only on the distance between atoms i and j. The many-body part of the potential takes the same form as that proposed by Mendelev *et al.* [86] and Ackland *et al.* [87],

$$F(\rho_i)=-\sqrt{\rho_i}+\phi\rho_i^2, \tag{A2}$$

where ϕ is a parameter. The effective electron density ρ_i is defined in a way slightly different from the conventional EAM potential. We write

$$\rho_i=\sum_j t_{ij}^2, \tag{A3}$$

where $t_{ij}=t_{ij}(R_{ij})$ is a pairwise hopping integral, which we take as a function of the distance between the atoms R_{ij}. We note that the derivative of ρ_i with respect to R_{ij} is

$$\frac{\partial\rho_i}{\partial R_{ij}}=2t_{ij}\frac{\partial t_{ij}}{\partial R_{ij}}. \tag{A4}$$

t_{ij} and V_{ij} are given by the third-order splines

$$t_{ij}(x)=\sum_n t_n\left(r_n^t-x\right)^3\Theta\left(r_n^t-x\right), \tag{A5}$$

$$V_{ij}(x)=\sum_n V_n\left(r_n^V-x\right)^3\Theta\left(r_n^V-x\right), \tag{A6}$$

where n are the knots, t_n, V_n are the parameters with dimensionality eV Å^{-3}, and r_n^t and r_n^V are given in angstroms. Their values are given in Table I.

APPENDIX B: EXCHANGE COUPLING AND LANDAU COEFFICIENTS

The exchange coupling function and Landau coefficients, expressed as functions of electron density, have different functional forms in bcc and fcc cases. In the bcc case, we use the following form:

$$J_{ij}(r_{ij})=J_0(1-r_{ij}/r_{\text{cut}})^5, \tag{B1}$$

$$A(\rho_i)=a_0+a_1\rho_i+a_2\rho_i^2, \tag{B2}$$

$$B(\rho_i)=b_0+b_1\rho_i+b_2\rho_i^2. \tag{B3}$$

In the fcc case, we take

$$J_{ij}(r_{ij})=J_0\sin(br_{ij}+c)(1-r_{ij}/r_{\text{cut}})^3, \tag{B4}$$

$$A(\rho_i)=a_0(1-\rho_i/\rho_a)^3+a_1, \tag{B5}$$

$$B(\rho_i)=b_0(1-\rho_i/\rho_b)^3+b_1. \tag{B6}$$

J_{ij}, A, and B are given in eVμ_B^{-2}, eVμ_B^{-2}, and eVμ_B^{-4} units, respectively. The cutoff distance r_{cut} is given in angstroms. All the parameters are listed in Table II.

TABLE I. Parameters of the nonmagnetic iron potential.

ϕ	$-4.48307570229369801\times10^{-4}$
r_0^t	$2.0000000000000000\times10^{0}$
r_1^t	$2.2000000000000000\times10^{0}$
r_2^t	$2.6000000000000000\times10^{0}$
r_3^t	$3.2000000000000000\times10^{0}$
r_4^t	$3.8000000000000000\times10^{0}$
r_5^t	$4.6000000000000000\times10^{0}$
r_6^t	$5.3000000000000000\times10^{0}$
t_0	$2.5999782982854347\times10^{0}$
t_1	$2.9319480072508499\times10^{0}$
t_2	$-2.8388905185188360\times10^{0}$
t_3	$-1.0267419494754382\times10^{-1}$
t_4	$1.5484736035888333\times10^{-2}$
t_5	$-7.2805743511785065\times10^{-2}$
t_6	$-3.6343523861565924\times10^{-3}$
r_0^V	$2.3254531341916498\times10^{0}$
r_1^V	$2.3889005055990276\times10^{0}$
r_2^V	$2.5614990650026459\times10^{0}$
r_3^V	$2.5615004425308658\times10^{0}$
r_4^V	$2.8344513929093051\times10^{0}$
r_5^V	$2.8321879787700808\times10^{0}$
r_6^V	$2.6382534884695783\times10^{0}$
r_7^V	$3.4262631740080707\times10^{0}$
r_8^V	$3.8479639767860356\times10^{0}$
r_9^V	$3.8515517885908994\times10^{0}$
r_{10}^V	$4.3740210397021579\times10^{0}$
r_{11}^V	$4.4054035197078845\times10^{0}$
r_{12}^V	$4.5503412747697087\times10^{0}$
r_{13}^V	$4.7731075757035732\times10^{0}$
r_{14}^V	$5.3000000000000000\times10^{0}$
V_0	$2.2831054190426084\times10^{1}$
V_1	$-2.1062362139531867\times10^{1}$
V_2	$5.6190823955741749\times10^{0}$
V_3	$8.0795758060570382\times10^{0}$
V_4	$-8.5213153270399573\times10^{1}$
V_5	$9.0355710040623180\times10^{1}$
V_6	$-8.3613137262443793\times10^{0}$
V_7	$-3.4250845501053456\times10^{-1}$
V_8	$5.2035042290453923\times10^{1}$
V_9	$-5.1583785613198948\times10^{1}$
V_{10}	$4.0569674844835752\times10^{0}$
V_{11}	$-5.0779874829818361\times10^{0}$
V_{12}	$1.7323802861372730\times10^{0}$
V_{13}	$-3.5971267571846299\times10^{-1}$
V_{14}	$-1.1478647839739256\times10^{-1}$

APPENDIX C: SYSTEMIC ERROR IN FORWARD AND BACKWARD ADIABATIC SWITCHING

Adiabatic switching samples through a sequence of nonequilibrium states. It estimates the free energy difference

TABLE II. Parameters for exchange coupling and Landau coefficients.

bcc	
J_0	$1.7613094778950000\times10^{-1}$
$r_{\rm cut}$	$5.3000000000000000\times10^{0}$
a_0	$-2.3827723674043900\times10^{-1}$
a_1	$1.2945703172205700\times10^{-2}$
a_2	$-1.1518969922985000\times10^{-4}$
b_0	$1.0600315078586900\times10^{-2}$
b_1	$1.6104913287021000\times10^{-3}$
b_2	$-4.3178188078544200\times10^{-5}$
fcc	
J_0	$1.1095507874951400\times10^{-1}$
$r_{\rm cut}$	$5.3000000000000000\times10^{0}$
b	$1.6502332463388100\times10^{0}$
c	$-4.1373722623161200\times10^{0}$
a_0	$3.1803486683085200\times10^{-1}$
a_1	$6.0141682907976200\times10^{-2}$
ρ_a	$2.2852502987397700\times10^{1}$
b_0	$1.4290243674270400\times10^{-2}$
b_1	$0.0000000000000000\times10^{0}$
ρ_b	$3.2563330708156800\times10^{1}$

δF by calculating the irreversible work $W_{\rm irr}$ done during the switching process [66,67]:

$$W_{\rm irr}=\int_0^{t_{\rm tot}}\frac{\partial\mathcal{H}_{ti}}{\partial\lambda}\frac{\partial\lambda}{\partial t}dt. \tag{C1}$$

It is a biased estimate of the reversible work done $W_{\rm rev}=\delta F$, which is the free energy difference between the initial and final states. Due to the irreversible nature of the nonequilibrium process involved, a systematic error is introduced, which is

$$W_{\rm irr}=W_{\rm rev}+\Delta E_{\rm diss}, \tag{C2}$$

where $\Delta E_{\rm diss}$ is the amount of dissipated heat caused by dissipative entropy production. It has been proven that $\Delta E_{\rm diss}$ is positive definite, and equals to the dissipative heat generated if the switching is in the opposite (or backward) direction provided that the energy distribution during the nonequilibirum process is close enough to the energy distribution at equilibrium, where the linear-response theorem applies [67]. One can write

$$W_{\rm irr}^{i\to f}=W_{\rm rev}+\Delta E_{\rm diss}, \tag{C3}$$

$$W_{\rm irr}^{f\to i}=-W_{\rm rev}+\Delta E_{\rm diss}, \tag{C4}$$

such that the reversible work done is

$$W_{\rm rev}=\tfrac{1}{2}\left(W_{\rm irr}^{i\to f}-W_{\rm irr}^{f\to i}\right). \tag{C5}$$

This eliminates the systematic error by means of forward and backward switching. If the switching process is only performed in a single direction, one should provide an estimate for $\Delta E_{\rm diss}$.

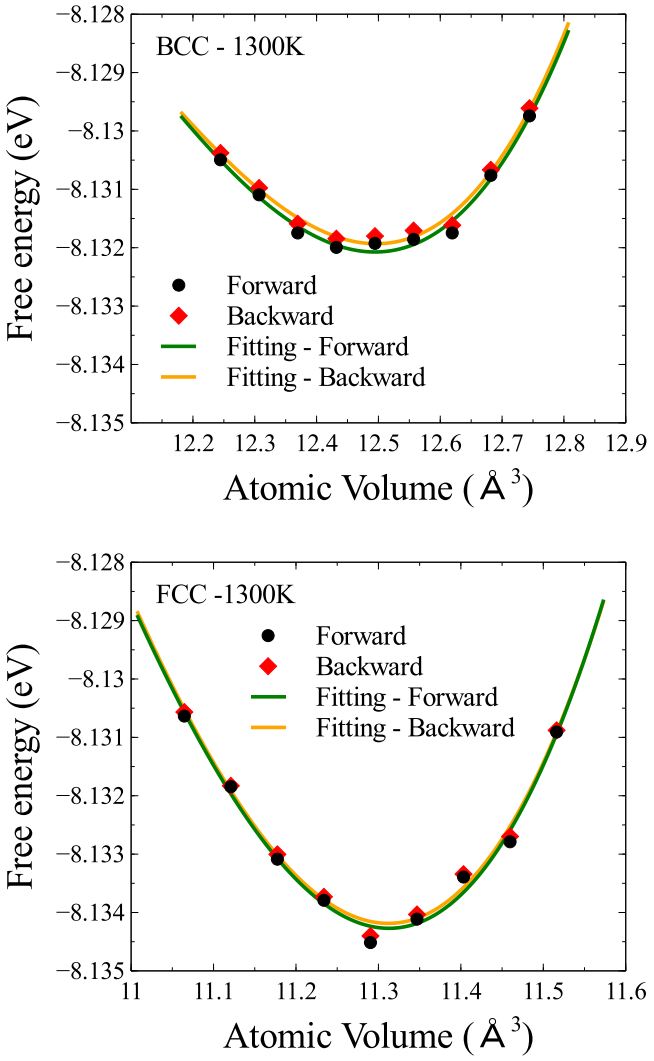

FIG. 18. Free energies of bcc and fcc iron as functions of atomic volume at $T=1300$ K. They are calculated using forward and backward switching. The fitted curves are third-order polynomials. We used the same parameters in Figs. 12 and 13.

All the results given in this paper were computed using the forward switching only. We now evaluate the systematic error to ensure the correctness of our conclusion. We performed a backward switching calculation at 1300 K using exactly the same parameters as those used for producing data shown in Figs. 12 and 13. Similarly to Fig. 1, we plot the Helmholtz free energy versus atomic volume for both bcc and fcc cases in Fig. 18. The y axis in the two figures have the same scale. We see that the difference between the values computed using forward and backward switching is significantly smaller than the free energy difference between bcc and fcc phases. The free energy of the fcc phase is still lower than the bcc phase by 2 meV per atom.

All the values computed using backward switching are offset upwards by no more than 0.15 meV. At the bottom of the third order polynomial fitted curves, they differ by 0.14 meV in the bcc case and 0.08 meV in the fcc case. It turns out that the effect of dissipative heat changes our conclusion by approximately $(0.14-0.08)/2=0.03$ meV per atom, which

is two orders of magnitude smaller than the calculated free energy difference between bcc and fcc phases, i.e., 2 meV per atom, and is an order of magnitude smaller than the fitting error [Fig. 14(b)]. Hence we are able to conclude that the systematic error is negligible and does not affect the accuracy of our simulations.

[1] H. Hasegawa and D. G. Pettifor, Phys. Rev. Lett. **50**, 130 (1983).
[2] J. Neuhaus, M. Leitner, K. Nicolaus, W. Petry, B. Hennion, and A. Hiess, Phys. Rev. B **89**, 184302 (2014).
[3] M. Yu. Lavrentiev, D. Nguyen-Manh, and S. L. Dudarev, Comput. Mater. Sci. **49**, S199 (2010).
[4] M. Yu. Lavrentiev, D. Nguyen-Manh, and S. L. Dudarev, Phys. Rev. B **81**, 184202 (2010).
[5] H. C. Herper, E. Hoffmann, and P. Entel, Phys. Rev. B **60**, 3839 (1999).
[6] R. Soulairol, C.-C. Fu, and C. Barreteau, J. Phys.: Condens. Matter **22**, 295502 (2010).
[7] D. Nguyen-Manh and S. L. Dudarev, Phys. Rev. B **80**, 104440 (2009).
[8] S. Alnemrat, J. P. Hooper, I. Vasiliev, and B. Kiefer, J. Phys.: Condens. Matter **26**, 046001 (2014).
[9] G. Autés, C. Barreteau, D. Spanjaard, and M.-C. Desjonquéres, J. Phys.: Condens. Matter **18**, 6785 (2006).
[10] M. E. A. Coury, S. L. Dudarev, W. M. C. Foulkes, A. P. Horsfield, Pui-Wai Ma, and J. S. Spencer, Phys. Rev. B **93**, 075101 (2016).
[11] F. Körmann, T. Hickel, and J. Neugebauer, Curr. Opin. Solid State Mater. Sci. **20**, 77 (2016).
[12] S. V. Okatov, A. R. Kuznetsov, Yu. N. Gornostyrev, V. N. Urtsev, and M. I. Katsnelson, Phys. Rev. B **79**, 094111 (2009).
[13] V. I. Razumovskiy, A. V. Ruban, and P. A. Korzhavyi, Phys. Rev. Lett. **107**, 205504 (2011).
[14] S. Polesya, S. Mankovsky, D. Ködderitzsch, J. Minár, and H. Ebert, Phys. Rev. B **93**, 024423 (2016).
[15] S. Mankovsky, S. Polesya, H. Ebert, W. Bensch, O. Mathon, S. Pascarelli, and J. Minár, Phys. Rev. B **88**, 184108 (2013).
[16] I. Leonov, A. I. Poteryaev, V. I. Anisimov, and D. Vollhardt, Phys. Rev. Lett. **106**, 106405 (2011).
[17] I. Leonov, A. I. Poteryaev, V. I. Anisimov, and D. Vollhardt, Phys. Rev. B **85**, 020401 (2012).
[18] I. Leonov, A. I. Poteryaev, Yu. N. Gornostyrev, A. I. Lichtenstein, M. I. Katsnelson, V. I. Anisimov, and D. Vollhardt, Sci. Rep. **4**, 5585 (2014).
[19] F. Körmann, A. Dick, B. Grabowski, B. Hallstedt, T. Hickel, and J. Neugebauer, Phys. Rev. B **78**, 033102 (2008).
[20] F. Körmann, A. Dick, T. Hickel, and J. Neugebauer, Phys. Rev. B **79**, 184406 (2009).
[21] F. Körmann, A. Dick, T. Hickel, and J. Neugebauer, Phys. Rev. B **81**, 134425 (2010).
[22] A. V. Ruban and V. I. Razumovskiy, Phys. Rev. B **85**, 174407 (2012).
[23] V. P. Antropov, M. I. Katsnelson, M. van Schilfgaarde, and B. N. Harmon, Phys. Rev. Lett. **75**, 729 (1995).
[24] V. P. Antropov, M. I. Katsnelson, B. N. Harmon, M. van Schilfgaarde, and D. Kusnezov, Phys. Rev. B **54**, 1019 (1996).
[25] O. Ivanov and V. Antropov, J. Appl. Phys. **85**, 4821 (1999).
[26] M. Fähnle, R. Drautz, R. Singer, D. Steiauf, and D. V. Berkov, Comput. Mater. Sci. **32**, 118 (2005).
[27] P.-W. Ma and S. L. Dudarev, Phys. Rev. B **91**, 054420 (2015).
[28] Ph. Kurz, F. Förster, L. Nordström, G. Bihlmayer, and S. Blügel, Phys. Rev. B **69**, 024415 (2004).
[29] R. Singer, M. Fähnle, and G. Bihlmayer, Phys. Rev. B **71**, 214435 (2005).
[30] B. Újfalussy, X.-D. Wang, D. M. C. Nicholson, W. A. Shelton, G. M. Stocks, Y. Wang, and B. L. Györffy, J. Appl. Phys. **85**, 4824 (1999).
[31] G. M. Stocks, B. Újfalussy, X.-D. Wang, D. M. C. Nicholson, W. A. Shelton, Y. Wang, A. Canning, and B. L. Györffy, Philos. Mag. B **78**, 665 (1998).
[32] P. H. Dederichs, S. Blügel, R. Zeller, and H. Akai, Phys. Rev. Lett. **53**, 2512 (1984).
[33] Pui-Wai Ma and S. L. Dudarev, Phys. Rev. B **83**, 134418 (2011).
[34] Pui-Wai Ma and S. L. Dudarev, Phys. Rev. B **86**, 054416 (2012).
[35] A. V. Ruban, S. Khmelevskyi, P. Mohn, and B. Johansson, Phys. Rev. B **75**, 054402 (2007).
[36] A. V. Ruban, A. B. Belonoshko, and N. V. Skorodumova, Phys. Rev. B **87**, 014405 (2013).
[37] F. Körmann, A. Dick, B. Grabowski, T. Hickel, and J. Neugebauer, Phys. Rev. B **85**, 125104 (2012).
[38] F. Körmann, B. Grabowski, B. Dutta, T. Hickel, L. Mauger, B. Fultz, and J. Neugebauer, Phys. Rev. Lett. **113**, 165503 (2014).
[39] T. Lee, M. I. Baskes, S. M. Valone, and J. D. Doll, J. Phys.: Condens. Matter **24**, 225404 (2012).
[40] L. Malerba, M. C. Marinica, N. Anento, C. Bjrkas, H. Nguyen, C. Domain, F. Djurabekova, P. Olsson, K. Nordlund, A. Serra, D. Terentyev, F. Willaime, and C. S. Becquart, J. Nucl. Mater. **406**, 19 (2010).
[41] M.-C. Marinica, F. Willaime, and J.-P. Crocombette, Phys. Rev. Lett. **108**, 025501 (2012).
[42] P. Olsson, J. Wallenius, C. Domain, K. Nordlund, and L. Malerba, Phys. Rev. B **72**, 214119 (2005).
[43] P. Olsson, J. Wallenius, C. Domain, K. Nordlund, and L. Malerba, Phys. Rev. B **74**, 229906(E) (2006).
[44] S. L. Dudarev and P. M. Derlet, J. Phys.: Condens. Matter **17**, 7097 (2005).
[45] P. M. Derlet and S. L. Dudarev, Prog. Mater. Sci. **52**, 299 (2007).
[46] G. J. Ackland, J. Nucl. Mater. **351**, 20 (2006).
[47] C.-S. Lian, J.-T. Wang, and C. Chen, Phys. Rev. B **92**, 184110 (2015).
[48] B. Alling, F. Körmann, B. Grabowski, A. Glensk, I. A. Abrikosov, and J. Neugebauer, Phys. Rev. B **93**, 224411 (2016).
[49] P.-W. Ma, C. H. Woo, and S. L. Dudarev, AIP Conf. Proc. **999**, 134 (2008).
[50] P.-W. Ma, C. H. Woo, and S. L. Dudarev, Phys. Rev. B **78**, 024434 (2008).
[51] P.-W. Ma, S. L. Dudarev, A. A. Semenov, and C. H. Woo, Phys. Rev. E **82**, 031111 (2010).
[52] S. Chandrasekhar, Rev. Mod. Phys. **15**, 1 (1943).
[53] R. Kubo, Rep. Prog. Phys. **29**, 255 (1966).
[54] H. Wen, P.-W. Ma, and C. H. Woo, J. Nucl. Mater. **440**, 428 (2013).
[55] H. Wen and C. H. Woo, J. Nucl. Mater. **455**, 31 (2014).

[56] P.-W. Ma, C. H. Woo, and S. L. Dudarev, Philos. Mag. **89**, 2921 (2009).
[57] D. Beaujouan, P. Thibaudeau, and C. Barreteau, Phys. Rev. B **86**, 174409 (2012).
[58] P. Thibaudeau and D. Beaujouan, Physica A (Amsterdam) **391**, 1963 (2012).
[59] D. Perera, D. P. Landau, D. M. Nicholson, G. M. Stocks, M. Eisenbach, J. Q. Yin, and G. Brown, J. Appl. Phys. **115**, 17D124 (2014).
[60] D. Perera, M. Eisenbach, D. M. Nicholson, G. M. Stocks, and D. P. Landau, Phys. Rev. B **93**, 060402 (2016).
[61] T. D. Swinburne, P.-W. Ma, and S. L. Dudarev, New J. Phys. **19**, 073024 (2017).
[62] G. M. Torrie and J. P. Valleau, J. Comp. Phys. **23**, 187 (1977).
[63] J. G. Kirkwood, J. Chem. Phys. **3**, 300 (1935).
[64] D. Frenkel and A. J. C. Ladd, J. Chem. Phys. **81**, 3188 (1984).
[65] G. Ciccotti, D. Frenkel, and I. R. McDonald, *Simulation of Liquids and Solids: Molecular Dynamics and Monte Carlo Methods in Statistical Mechanics* (North-Holland, Amsterdam, 1987).
[66] R. Freitas, M. Asta, and M. de Koning, Comput. Mater. Sci. **112**, 333 (2016).
[67] M. de Koning, J. Chem. Phys. **122**, 104106 (2005).
[68] M. de Koning and A. Antonelli, Phys. Rev. E **53**, 465 (1996).
[69] P.-W. Ma, S. L. Dudarev, and C. H. Woo, Comput. Phys. Commun. **207**, 350 (2016).
[70] U. Gonser, C. J. Meechan, A. H. Muir, and H. Wiedersich, J. Appl. Phys. **34**, 2373 (1963).
[71] G. J. Johanson, M. B. McGirr, and D. A. Wheeler, Phys. Rev. B **1**, 3208 (1970).
[72] P. Brommer, A. Kiselev, D. Schopf, P. Beck, J. Roth, and H.-R. Trebin, Modell. Simul. Mater. Sci. Eng. **23**, 074002 (2015).
[73] P. Brommer and F. Gähler, Modell. Simul. Mater. Sci. Eng. **15**, 295 (2007).
[74] P. Brommer and F. Gähler, Philos. Mag. **86**, 753 (2006).
[75] F. Ercolessi and J. B. Adams, Europhys. Lett. **26**, 583 (1994).
[76] G. Kresse and J. Hafner, Phys. Rev. B **47**, 558 (1993).
[77] G. Kresse and J. Hafner, Phys. Rev. B **49**, 14251 (1994).
[78] G. Kresse and J. Furthmüller, Comput. Mat. Sci. **6**, 15 (1996).
[79] G. Kresse and J. Furthmüller, Phys. Rev. B **54**, 11169 (1996).
[80] J. P. Perdew, K. Burke, and M. Ernzerhof, Phys. Rev. Lett. **77**, 3865 (1996).
[81] J. P. Perdew, K. Burke, and M. Ernzerhof, Phys. Rev. Lett. **78**, 1396 (1997).
[82] S. V. Okatov, Yu. N. Gornostyrev, A. I. Lichtenstein, and M. I. Katsnelson, Phys. Rev. B **84**, 214422 (2011).
[83] R. Singer, F. Dietermann, and M. Fähnle, Phys. Rev. Lett. **107**, 017204 (2011).
[84] A. I. Liechtenstein, M. I. Katsnelson, V. P. Antropov, and V. A. Gubanov, J. Magn. Magn. Mater. **67**, 65 (1987).
[85] M. van Schilfgaarde and V. P. Antropov, J. Appl. Phys. **85**, 4827 (1999).
[86] M. I. Mendelev, D. J. Srolovitz, G. J. Ackland, D. Y. Sun, and M. Asta, Philos. Mag. **83**, 3977 (2003).
[87] G. J. Ackland, M. I. Mendelev, D. J. Srolovitz, S. Han, and A. V. Barashev, J. Phys:. Condens. Matter **16**, S2629 (2004).